CENTRO DE INVESTIGACIONES
EN OPTICA, A.C.

“THE DEVELOPMENT OF NEW MATERIALS FOR PHOTOCATALYTIC HYDROGEN GENERATION”

Thesis to obtain the degree of Doctor of Science (optics)

Student: M.C. Takawira Joseph Mumanga

Supervisor: Dr. Luis Armando Díaz Torres

León · Guanajuato · México

May 2021

Preface

Abstract

This work presents the development, characterization, and evaluation of 2D materials and Alkaline Metal Aluminates, namely Graphitic Carbon Nitrides (g-C_3N_4) and Barium or Magnesium Aluminates (MAl_2O_4: M=Ba or Mg) for the purpose of hydrogen generation. Graphitic carbon nitrides were synthesized by calcinating nitrogen-rich precursors at 550 °C whilst the alkaline metal aluminates were prepared by a combustion synthesis and were annealed in different gas atmospheres.

The characterization of these photocatalysts was carried out through techniques such as X-ray diffraction (XRD), Scanning Electron Microscopy (SEM), Diffuse Reflectance Spectroscopy (DRS), Energy Dispersive Spectroscopy (EDS), Raman Spectroscopy (RS), Brunauer-Emmett-Teller (BET) surface area analysis, Diffuse Reflectance Spectroscopy (DRS), Photoluminescence measurements (PL), and Electrochemical Impedance Spectroscopy (EIS).

The g-C_3N_4 photocatalysts were evaluated comparatively in Hydrogen Evolution Reactions (HERs) using irradiation from either low-cost visible (405 nm or 440 nm) 15 W/m LED strips or from a UV (254 nm, 4.4 mW/cm^2) pencil lamp. A high hydrogen production rate of 1622 $mol.g^{-1}.h^{-1}$, corresponding to an AQY of 3.2%, was achieved under UV irradiation using g-C_3N_4 p-n homojunction which was synthesized from Thiourea. The same irradiation source rendered a maximum H_2 generation rate of 97 $\mu mol.h^{-1}.g^{-1}$ using the carbon annealed magnesium aluminates. The overall results of these studies reveal the potential of these photocatalysts and major photocatalysis enhancement strategies based on conductivity modulation and heat treatment.

Table of Contents

List of Acronyms

XRD – X-ray diffraction

SEM – Scanning Electron Microscopy

EDS – Energy Dispersive Spectroscopy

BET – Brunauer-Emmett Teller

DRS - Diffuse Reflectance Spectroscopy

EIS – Electrochemical Impedance Spectroscopy

NHE - Normal Hydrogen Electrode

M-S - Mott–Schottky

FLS – Fluorescence Spectroscopy

UVviS - Ultraviolet-visible Spectroscopy

UCN – Urea derived Graphitic Carbon Nitride

TCN – Thiourea derived Graphitic Carbon Nitride

AQY - Apparent Quantum Yield

LED – Light Emitting Diodes

BCC – Carbon atmosphere Calcined Barium Aluminates

BAC – Air Calcined Barium Aluminates

MCC – Carbon atmosphere Calcined Magnesium Aluminates

MAC – Air Calcined Magnesium Aluminates

MB - Methylene Blue

NMR – Nuclear Magnetic Resonance

HER - Hydrogen Evolution Reaction

Index of Figures

Index of Tables

Acknowledgements

My personal declaration reads, “My life and its fruit are an honor to the almighty God”.

For having played a major role in the success of this work. I would like to thank the following:

My wife Maria Eugenia Soto and daughter Elisa Mumanga Soto;

My family and friends in Mexico and abroad for their support.

Dr. Luis Armando Díaz Torres, for his supervisión and guidance.

Dr. Eduardo Montes, Dr. Christian Gómez Solís, Dr. Carlos Pineda, Dr. Carlos Rodriguez

(Insight Mentorship)

María Christian Albor Cortés, Dr. María Rosario Galindo González

(Technical Assistance)

Universidad de Guanajuato Facultad de Química for their Potentiometer that was used to carry out measurements of Electrochemical Impedance Spectroscopy

CONACYT

(Scholarship No: 590749)

The Centro de Investigaciones en Optica, A.C., at both Leon and Aguascalientes campus for its facilities, equipment and financial support for carrying out all the experimental tasks and correspondence responsibilities.

Chapter 1 - Introduction

1.1 Hydrogen Utility and Generation

1.1.1 Need for Hydrogen

Hydrogen can replace fossil fuels, as such, it is referred to as 'the fuel of the future'[1]. Due to the rapid increase of the world's population and the expansion of modern technology, future energy forecasts confirm that there may exist an energy crisis caused by the imbalance between energy demand and its supply[2]. Hydrogen is regarded as an inexpensive source of energy and the key solution to the 21st century energy crisis[3].

Apart from its electrochemical reaction with oxygen, which could generate electricity, heat, and water as a by-product[4], hydrogen has several other uses. Hydrogen is used, among other applications, in metal embrittlement[5], petroleum refining[6] as well as the making of fertilizers, disinfectants, nitric acid, refrigerants[7], and preservative agents[8,9].

1.1.2 Hydrogen Production

Hydrogen is produced by electrolysis, thermolysis (steam reforming), biochemical methods, and photocatalysis[10]. The latter has become an exponentially growing area of research since the pioneering work of Honda and Fujishima in 1972[11]. Leading to this discovery, they noticed that titanium dioxide absorbed light energy and facilitated the breakdown of water into hydrogen and oxygen. Today, energy efficiencies of photocatalytic conversions are being enhanced by exploring novel materials and material modification[12].

1.1.3 Light

Various light sources have been used for photocatalysis experiments, these include the sun[13], sun simulators[14], fluorescent lamps[15], gas-discharge lamps[16], and LEDs[17]. Using Apparent Quantum Yield (AQY) calculations, these distinct light sources could be compared in their efficacy to drive photocatalytic hydrogen generation. The use of LEDs in photocatalysis has very fewer reports let alone LED strips. In this work, we use either low power-consumption LED strips or a low power UV pencil lamp to provide visible and UV light, respectively as shown in Figure 1.1.

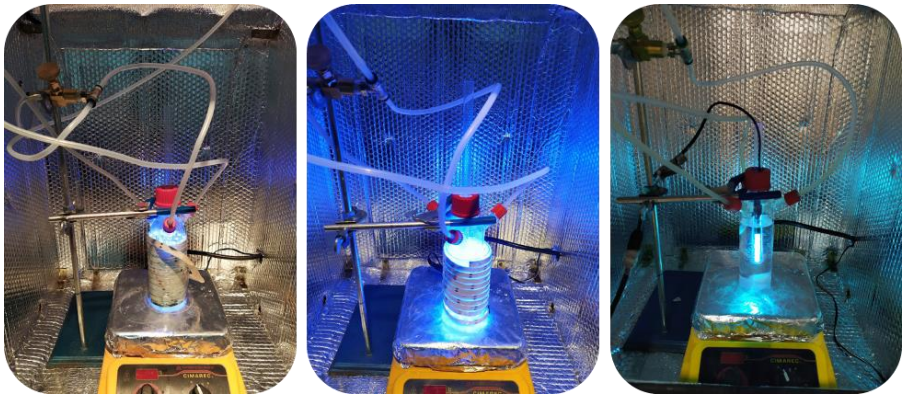

Figure 1.1 - Light sources used in this work

1.2 Wastewater Treatment

1.2.1 Dye Degradation

The widespread of organic dyes from industrial wastewater to the ecosystem is a dramatic source of pollution, eutrophication, and concern for aquatic life[18]. Some dyes and their metabolic intermediates are mutagenic and carcinogenic[19] The photocatalytic degradation of organic compounds and hydrogen generation are amongst the most important branches within the broader subject of photocatalysis. Semiconductor materials are ideal initiators and accelerators of the redox chemical reactions behind photocatalysis[20]. The quest has been and still is, to find less expensive, effective, and environmentally friendly photocatalytic materials.

1.3 Objectives and Motivation of this work

1.3.1 Overall Objective

To synthesize, characterize and evaluate new materials for photocatalytic hydrogen production.

1.3.1.1 Synthesis

To prepare graphitic carbon nitride by calcination from urea and thiourea precursors.

- To prepare barium and magnesium based alkaline earth metal aluminates by combustion synthesis and to thermally treat them in either air or carbon atmospheres.

1.3.1.1 Characterization

- To study the structural, morphological, optoelectrical and photoluminescence properties of graphitic carbon nitrides along with the examination of the effect of each precursor.
- To study the structural, morphological, optoelectrical and photoluminescence properties of alkaline earth metal aluminates along with the examination of the effect of heat treatment atmosphere.

1.3.1.1 Evaluation

- To test graphitic carbon nitrides as photocatalysts of a hydrogen evolution reaction under UV and visible light.
- To test alkaline earth metal aluminates as photocatalysts of a hydrogen evolution reaction under UV light irradiation.

1.3.2 Motivation

Advancement in the research area of photocatalytic hydrogen generation is stimulated by the constant production and evaluation of new materials with enhanced photocatalytic properties. This novelty is often a result of stoichiometric and synthesis modifications. The immediate goal for most researchers is to achieve higher hydrogen evolution quantum efficiencies to commercialize the photocatalytic hydrogen generation systems. The motivation of this work is to contribute a new report on the study of parallel sets of semiconductor photocatalysts with distinct properties and demonstrated photocatalytic process enhancements.

Chapter 2 - Background

2.1 Graphitic Carbon Nitride (g-C_3N_4)

2.1.1 Introduction

Graphitic carbon nitride (g-C_3N_4) has attracted the interest of many researchers in the past decade. Represented in Figure 2.1, g-C_3N_4 is a two-dimensional graphite-like layered polymer, that is sought for its visible light absorption, mild bandgap, and chemical stability[21]. Graphitic carbon nitride is generally prepared through the thermal condensation of nitrogen-rich precursors such as thiourea, dicyandiamide, melamine, and urea[22–25].

Unfortunately, pure g-C_3N_4 suffers high charge carrier recombination and is therefore considered as a poor photocatalyst. As such, in order to, harness its strengths, g-C_3N_4 has been the essential matrix for recent composites of heterojunction, co-catalyst, or nanocarbon loading designs[26]. Amongst the vast efforts of enhancement, conductivity modulation of g-C_3N_4 has fewer reports.

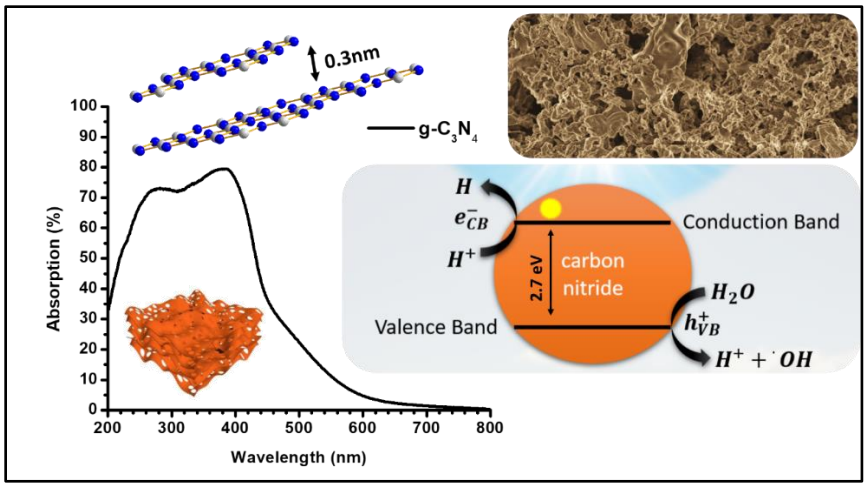

Figure 2.1 - Structure and Absorption properties of g-C_3N_4

2.1.2 Similar Work

2.1.2.1 Conductivity

The extreme case of conductivity modulation implies a total switch of behavior from the common n-type g-C_3N_4 to p-type g-C_3N_4. This is often achieved through the introduction of impurity electron donors or acceptors[27]. Wang et. al. successfully switched the conductivity of g-C_3N_4 from n-type to p-type by doping g-C_3N_4 with chloride ions so as to form acceptor states[28].

Xu et. al. synthesized p-type g-C_3N_4 under an ammonia (NH_3) self-generated atmosphere and co-doping it with K and Fe[29]. Chen et. al also prepared p-type g-C_3N_4 by co-doping it with K and I[30]. Such doping interventions have led to improved charge separation and transport properties as well as the suppression of charge recombination amongst other advantages[31].

The co-existence of n-type and p-type characteristics has also led to highly efficient separation and transfer of photogenerated charge carriers. It has been achieved without the introduction of impurities. Liu et. al. obtained g-C_3N_4 based p-n junctions through the defect modification of pristine g-C_3N_4. The latter was mixed with $NaBH_4$ under mild heating conditions. By doing so cyano groups (−C≡N) were introduced as electron acceptors. As a result, this defective g-C_3N_4 exhibited both n-type and p-type conductivities whilst enhancing photocatalytic hydrogen generation[32].

Cao et. al. also constructed g-C_3N_4 p-n homojunction by introducing nitrogen vacancies to n-type g-C_3N_4 through calcination in a hydrogen atmosphere[33]. Nitrogen vacancies lead to the formation of unpaired electrons in g-C_3N_4 that can capture photogenerated electrons and increase the number of photogenerated holes thereby increasing the concentration of holes over a local area[34–36].

2.1.2.2 Defects

Similarly carbon vacancies in g-C_3N_4 can also function as electron traps and consequently strengthen the local density of holes[37]. Wang et. al synthesized g-C_3N_4 consisting of carbon vacancies formed by calcination in an Argon atmosphere[38]. Luo et. al postulated that these vacancies are formed from the reaction between nitrogen linked carbon species of g-C_3N_4 and self-generated ammonia (NH_3) which produces nitrogen and methane gases[39].

Xu et. al. proved that, during the pyrolysis of thiourea, higher concentrations of self-generated gases, mainly NH_3, are released during calcination at higher heating rates[40]. It can therefore be assumed that direct heat calcination increases the concentration of NH_3 and accelerates its reaction with carbon species. Yang et. al, on the other hand, suggested that the same reaction produced hydrogen and hydrogen cyanide which also led to the formation of carbon vacancies[41].

There have been other reports on the modification of g-C_3N_4s by the formation of carbon vacancies which upon evaluation have enhanced the efficiencies of photocatalytic hydrogen generation whilst attributing the enhancement to improved charge separation and transport efficiency[42,43]. As far as we know, there has been no report directly linking the presence of carbon vacancies to the modification of conductivity in g-C_3N_4 without the use of dopants.

2.1.3 Present Work Summary

This work presents the achievement of g-C_3N_4 based p-n homojunction owing to the introduction of electron acceptors resulting from both the formation of carbon vacancies and cyano groups.

2.2 Alkaline Metal Aluminates ($BaAl_2O_4$, $MgAl_2O_4$)

2.2.1 $MgAl_2O_4$

Owing to its good chemical stability, surface basic sites, mechanical strength and high melting temperature, $MgAl_2O_4$, a spinel type material, has been identified as an excellent catalyst and catalyst support [44]. It is used for a great variety of organic reactions, such as petroleum processing, fine chemicals production, propane and butane dehydrogenation [44–46].

The photocatalytic activity of $MgAl_2O_4$ product has also been studied by performing the decomposition of Reactive Red Me 4BL dye under UV illumination or sunlight irradiation. The dye was photo-degraded by 90.0 % and 95.45% under UV and sunlight irradiation, respectively, within 5 hours [47]. Other similar attempts using other materials have been made, in particular, to study the photocatalytic oxidation of methylene blue [48–50].

2.2.2 $BaAl_2O_4$

$BaAl_2O_4$, on the other hand, is also of great interest in catalysis for its reusability and non-corrosiveness. It has been used in the treatment of air pollutions, preparation of humidity sensors and phosphor materials. In recent work [51], $BaAl_2O_4$ was prepared by solid state synthesis, annealed at 1300 °C for 6 hours and tested for photocatalytic hydrogen production. The result was a hydrogen production rate of 3 µmol.g^{-1} after 2 hours of reaction time.

2.2.3 Similar Work

2.2.3.1 Spinel oxide photocatalyst

Other spinel-type oxides such as $BaCr_2O_4$ [52], $NiFe_2O_4$ [53], $CaBi_2O_4$ [54], $ZnGa_2O_4$ [55,56], $ZnFe_2O_4$ [57,58] and $CuAl_2O_4$ [59] have been used as semiconductor photocatalysts in the degradation of organic compounds and/or the photocatalytic production of hydrogen. Various other methods for the preparation of spinels have been reported such as co-precipitation [60], sol–gel [61], sonochemical [62], microemulsion [63] and solution combustion [64]. The crystallinity of spinel products has been proven to depend on the annealing temperature [65,66]. The photoluminescence properties of various oxides including $MgAl_2O_4$ and $BaAl_2O_4$

have also been shown to be dependent on annealing temperature and the amount of oxygen vacancies [67–70].

2.2.3.2 Thermal Treatment

Most of the produced spinel are obtained and annealed under air atmosphere, annealing in air promotes the elimination of impurities, stabilization of the crystalline phase, and reduces the amount of oxygen vacancies or oxygen related defects within the crystalline structure. On the other hand, for photocatalytic purposes, the use of a reductive atmosphere might lead to an oxygen deficiency, and the related defects, in the crystalline lattice; increasing in that way the potential photocatalytic sites on the surface of the annealed spinel.

The most used reductive atmosphere consists of a mixture of H_2 and N_2 gasses, but its use presents some technical complications and security hazards due the use of H_2. A simpler and more economical option to have a reductive atmosphere in annealing treatments consist in the use of Carbon as the source of CO reductive radicals.

2.2.4 Present Work Summary

This work presents a unique comparison of the photocatalytic properties of $BaAl_2O_4$ and $MgAl_2O_4$ spinel-type materials annealed under either air or Carbon (gaseous C, CO) atmospheres.

Chapter 3 - Methodology

3.1 Synthesis Procedures

3.1.1 Synthesis of g-C_3N_4

Urea and thiourea (Karal ≥ 99% purity) were analytical grade and used without further treatment. An amount of 25g of either precursor was directly heated within a closed alumina crucible (with a lid weighing about 30g) at 550°C for 3 hours in air. It was then left to cool down to room temperature at an approximate rate of -4°C min^{-1}. The resultant material was ground into a fine powder and denoted as UCN, for the carbon nitride prepared from urea, or TCN, for the carbon nitride prepared from thiourea. As shown in Figure 3.1 UCN was yellowish with a product yield of 7% whilst TCN was reddish with a product yield of 25%.

Figure 3.1 - Synthesis Process and g-C3N4 Products

3.1.2 Synthesis of $BaAl_2O_4$ and $MgAl_2O_4$

Stoichiometric quantities of the reagents were added into a 250 ml *Pyrex* glass vessel and kept under magnetic stirring over a hot plate as presented in Figure 3.2. The reagents and precipitation agents included aluminum nitrate nonahydrate [$Al(NO_3)_3.9H_2O$], barium nitrate [$Ba(NO_3)_2$] or magnesium nitrate hexahydrate [$Mg(NO_3)_2.6H_2O$], ammonium nitrate [$NH_4(NO_3)$] as the oxidant, boric acid [H_3BO_3] as the flame retardant and urea [$CO(NH_2)_2$] as the fuel upon which the temperature of the solution drops drastically. The ratio of the oxidant to the fuel was 1:43. After 30 minutes of stirring, the solution was then inserted into an Oven, previously stabilized at 600°C, for 15 minutes. The maximum combustion

temperature is limited by the thermodynamics of the of the considered system reactions. It is in the range of 500K–4000K.

Figure 3.2 - Synthesis Procedure and spinel products

After cooling, the foamy product was milled in a mortar and one gram of the grinded powder was compressed into a pellet. Barium aluminate pellets were annealed in both air or carbon atmosphere at 1100°C for 2 hours whilst Magnesium aluminate pellets were annealed in either air or carbon atmosphere at 900°C for 1 hour. The products were abbreviated BCC, BAC, MCC and MAC where the first letter refers to barium or magnesium, CC stand for carbon atmosphere annealing, and AC stands for air atmosphere annealing. During air annealing, the pellets were placed in an open crucible whereas during carbon annealing the pellets were placed in a closed crucible and submerged into a larger closed crucible filled with carbon.

3.2 Structure and morphology

3.2.1 X-ray diffraction (XRD)

In order to identify the crystalline phase and compare the degree of structural order, X-ray diffraction (XRD) measurements of the powders were performed on a Bruker D2 phaser diffractometer with 1.54184 Å Cu-Kα radiation, with a swipe rate of 0.02°.

3.2.2 Scanning Electron Microscopy (SEM)

To study the particle morphology, characterization was performed by means of a JSM-7800F field emission scanning electron microscope (SEM). To prepare the samples for insertion into the SEM chamber, further grounding was done to produce a fine powder. A spatula tip of this powder was put into 1.5 ml of absolute ethanol and subjected to an

ultrasound bath for 30 minutes. Afterwards a droplet of this solution was put over a silicon substrate and left to dry at room temperature within a closed petri dish in the darkness.

3.2.3 Energy Dispersive Spectroscopy (EDS)

Energy Dispersive Spectroscopy (EDS) was accomplished inside the JSM-7800F field emission Scanning Electron Microscope (SEM). An Oxford Instruments X-Max 80 silicon drift detector was used to obtain the spectra.

3.2.4 Raman Spectroscopy

The Raman spectra, used to reveal the quality of the structure through the analysis of the vibrational modes, were recorded on an In Via Renishaw Raman microscope with an IR excitation laser of 785nm.

3.2.5 Brunauer-Emmett-Teller (BET) Analysis

Brunauer-Emmett-Teller (BET) surface area measurements were taken on a Quantachrome Instruments Autosorb- iQ-MP/XR surface area analyzer. The samples were degassed at 300°C before the measurement and a multi-point BET method was used with a relative pressure range (P/P_0) of 0.05-0.3.

3.2.6 Fourier Transform Infrared (FTIR) Spectroscopy

FTIR spectra were acquired using a Cary 670 FTIR coupled with a Cary 620 FTIR spectrometer from Agilent Technologies. The spectrometer consists of a Michelson Interferometer aligned at 60° with a spectral range of 400-4000cm-1 and a resolution of 0.075cm-1. Samples were introduced in powder form.

3.3 Photoelectronic Properties

3.3.1 Absorption Properties

UV-vis Diffuse Reflectance spectra (DRS) of the samples in powder form were recorded on a Cary 5000 UV-Vis-NIR spectrophotometer (Agilent Technologies). These results were then transformed to an absorbance scale from which the absorption coefficient could be determined. The optical bandgap of the samples was determined via the Tauc method using the DRS data. It was estimated following the expression [71],

$$(\alpha h\nu)^{\frac{1}{n}} = A(h\nu - E_g) \quad (1)$$

where $\boldsymbol{h}$ is Planck's constant, $\boldsymbol{\nu}$ is the frequency of vibration, $\boldsymbol{\alpha}$ is the absorption coefficient, $\boldsymbol{E_g}$ is the bandgap and $\boldsymbol{A}$ is a proportional constant. The exponent describes the nature of the

transition for which ***n = 1/2*** gave a better fit and corresponds to direct allowed electron transitions.

3.3.2 Photoluminescence

Photoluminescence measurements were taken on a modular Acton Research corporation fluorimeter equipped with a Xenon lamp and a monochromator which was set to allow the excitation wavelengths centered at 254 nm, 400 nm and 440 nm The powder samples were kept for more than 24 hours in darkness before measurements were taken.

3.3.3 Electronic Properties

The Electrochemical Impedance Spectroscopy (EIS) measurements, based on the Mott–Schottky (M–S) plot, were conducted on an SP-150 (SN 1044) potentiostat for Graphitic Carbon Nitride materials. In another case a VSP (SN 1355) as shown in Figure 3.3 potentiostat was used to carry out Electrochemical Impedance Spectroscopy (EIS) using the Mott Schottky method to determine the band edge potentials of the alkaline metal aluminates.

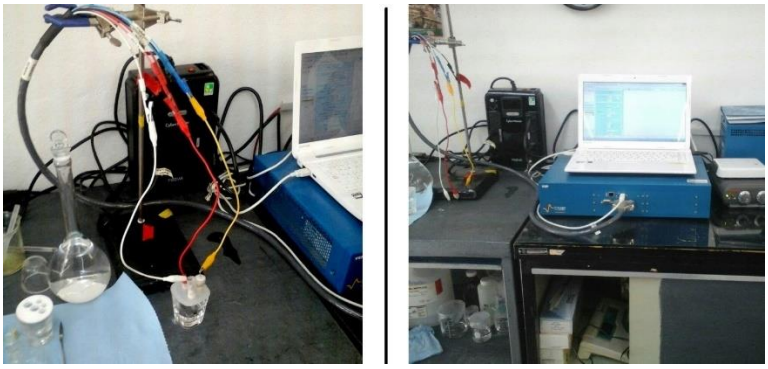

Figure 3.3 - VSP (SN 1355) potentiostat

The materials were embedded on glass electrodes and then placed into the oven at 300°C for 2 hours in order to ensure an efficient deposition of the material over the glass surface. A three-electrode configuration was utilized. Sodium Sulfate (Na_2SO_4) solution (0.5 M) was used as the solvent. The prepared glass electrodes served as the working electrodes (photo-anode), whilst a saturated Ag/AgCl was used as the reference electrode and a platinum coil functioned as the counter electrode. The Mott-Schottky relations for n-type and p-type semiconductors are described as [72],

$$\frac{1}{C_{sc}^2} = \frac{2}{\varepsilon\varepsilon_0 e N_D}\left(E - E_{fb} - \frac{k_B T}{e}\right) \quad (2)$$

$$\frac{1}{C_{sc}^2} = \frac{-2}{\varepsilon\varepsilon_0 e N_A}\left(E - E_{fb} + \frac{k_B T}{e}\right) \quad (3)$$

where C_{sc} is the space charge capacitance, ε is the dielectric constant of the semiconductor, ε_0 is the permittivity of free space, A is the area of the electrode, *e* is the elementary electric charge, N_D is the donor density, N_A is the acceptor density, E is the applied potential, E_{fb} is the position of the flat band potential, k is the Boltzman constant and T is the temperature.

All the measurements were carried out at a scanning frequency of 1 kHz to ensure that the charge transfer over the interface was small enough for both materials. The flat band potential could then be given if $1/C_{sc}^2$ is plotted against the applied potential as an extrapolated intercept with zero. Considering, that Ag/AgCl reference electrode is shifted 0.197 eV [73] with respect to the Normal Hydrogen Electrode (NHE), the band edge positions can be plotted using the flatband potential and the optical band gap results.

3.4 Dye Degradation Experiments

3.4.1 Equipment

The Newport, Oriel Sol3a solar simulator shown in Figure 3.4, was used as the photocatalysis light source. The degree of degradation was quantified by using the Agilent Technologies, Cary 60 UV-Vis spectrometer by analyzing the main absorption peak of methylene blue MB at 665 nm.

Figure 3.4 - Solar Simulator

3.4.2 Measures and Procedure

Aqueous solutions with 15 ppm of methylene blue (MB) were used as starting dye solutions to be photo-degraded. The volume value in *ml* of dye to be degraded was equal to the mass value of photocatalyst in *mg* to be added to it. Upon adding the photocatalyst, the mixture was thereafter bathed in ultrasound with the lid of the bath placed over the solution in order to minimize the exposure to light.

The bathing process lasted 20 minutes. Thereafter the solution was covered with aluminum foil and kept in the dark for 40 minutes. After the dark time treatment, the solution was distributed into 2.5 ml Eppendorf tubes. These tubes were subjected under a solar simulator with one tube withdrawn at 15-minute intervals.

Figure 3.5 - Eppendorf tubes subjected under the solar simulator

3.4.3 Degradation Rate

The results were presented as the degradation rate, C/C_0, where 'C_0' and 'C' are the absorption intensities of the solution at times 't_0' and 't' respectively. On the other hand, the degradation percentage (D %) is calculated as follows [74]:

$$D\ \% = (C_0\text{-}C)/C_0 \times 100 \qquad (2)$$

3.5 Hydrogen Generation Experiments

3.5.1 Equipment

The photocatalytic activity of UCN and TCN was evaluated in a pyrex glass reactor cell connected with a closed gas circulation system driven by a diaphragm pump. The cell was coupled to a Shimadzu Gas Chromatograph (GC 2014) with a TCD detector. The setup of the equipment is shown in Figure 3.6. During the reaction, it was illuminated by visible or UV light placed inside the interior of a quartz tube which was then inserted into the reactor.

The visible light was acquired from the use of 15 W/m SMD5050 Triple Core LED strips with principal wavelengths at 400nm or 442nm, placed in the form of a compressed spiral coil around the body of the glass reactor. The UV light was acquired from a mercury Pen-Ray lamp (UVP90001201, Thermo Fisher Scientific, USA) with a relative intensity of 4400 $\mu W/cm^2$ at a distance of 2 cm and a main wavelength centered at 254 nm. To further ensure that water vapor did not reach the chromatograph, a tightly sealed humidity filter with color-indicating silica gel was connected between the reactor and chromatograph.

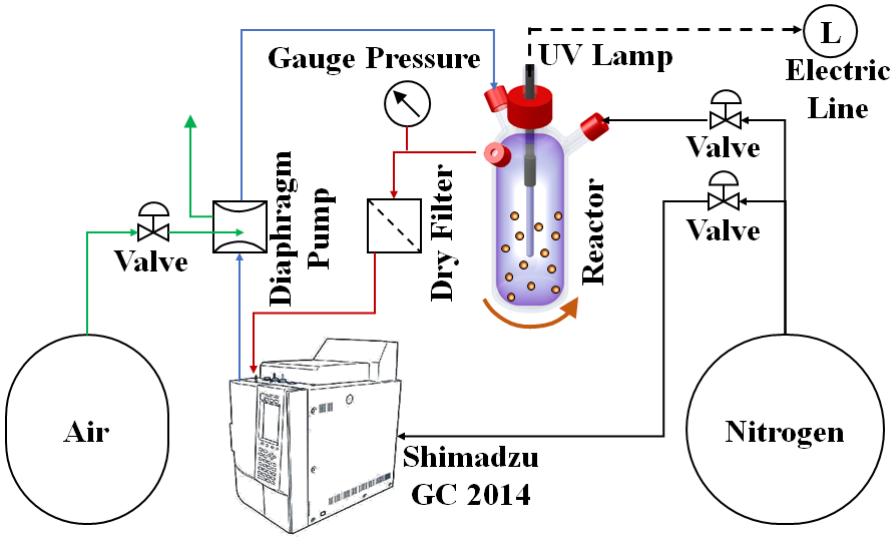

Figure 3.6 - Photocatalytic Hydrogen Evolution Experiment Setup

3.5.2 Measures and Procedure

The photocatalysts (5 mg) in the case of graphitic carbon nitride and (50 mg) in the case of the alkaline metal aluminates, were added into 200 mL of a 0.15 M (10% vol.) triethanolamine aqueous solution. The photocatalyst added solution was sonicated for 30 minutes in darkness before it was transferred into the reactor and maintained under mild stirring. The reactor cell was deoxygenated by bubbling-in nitrogen for at least 15 minutes before beginning the reaction. Then the HER was initiated by turning the light source on.

Reference measurement injections were made into the chromatograph during deoxygenation to ensure that zero hydrogen was detected before turning the illumination source on. Meanwhile the diaphragm pump was kept on, maintaining a steady flow and a uniform concentration of the gases throughout the system. Once the illumination was turned on, the generated hydrogen was recorded every 5 minutes with the precise support of programmable injection actuator in a one-hour experiment period.

3.5.3 Apparent Quantum Yield

To quantify and compare the performance of each photocatalyst under varied irradiation sources the apparent quantum yield was calculated according to the following equation [75]:

$$AQE\% = \frac{2 \times number\ of\ evolved\ H_2\ molecules}{number\ of\ incident\ photons} \times 100 \qquad (4)$$

or

$$AQE\% = \left(\frac{2 \times \beta \times N \times c \times h}{I \times S \times t \times \lambda \times 2\pi}\right) \times 100 \qquad (5)$$

where β is the quantity of evolved hydrogen (mol), N is Avogadro's number, c is the speed of light ($m.s^{-1}$), h is Planck's constant (Js), I is the irradiance of the source (W/cm^2), S is the surface area illuminated by the source (cm^2), t is the time of the reaction process (s) and λ is the wavelength of the illumination source (m).

3.6 Optimization Experiments

3.6.1 Optimization Experiment I

The experimental procedure and setup images are shown in Figure 3.7 to summarize the preparation and nature of the experiment. First a 45° angled reflector made from the reflective sheets was formed. A reflector was connected over the fiber optic cable collimator lens which was then connected over the end of the fiber optic cable. The angle was adjusted and evaluated by passing visible light through the fiber optic cable using the UV-vis light source. The fiber optic cable with the reflector was inserted into a pyrex glass test tube and then introduced into the 3-pin HER glass reactor.

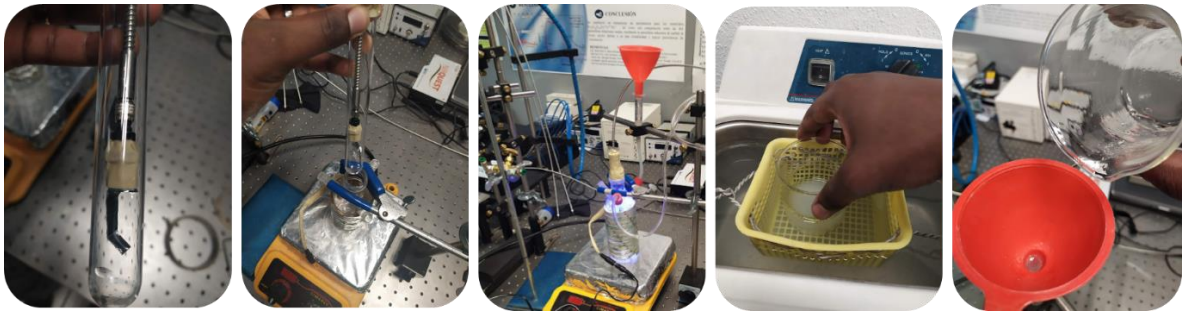

Figure 3.7 - Experimental Procedure and Setup Overview

Preliminary measurement conditions to study the degree of penetration of the source emission included the following:

- Single LED
- Empty Reactor (no medium)
- Water as Medium
- Water + TEOA

Thereafter the reactor and fiber optic cable detector were fixed so as to only vary the dispersion concentration determined by the amount of g-C_3N_4 (UCN) powder in the dispersion. To prepare a new concentration of the dispersion within the reactor, the desired weight of UCN was first measured and then mixed with a specific amount of dispersion extracted from the fixed reactor. This was agitated under a magnetic stirrer for 10 seconds, and then sonicated for 5 minutes, then stirred magnetically again for 10 seconds and finally poured into the reactor through a funnel.

The concentration that were prepared were 1mg/200ml, 5mg/200ml, 10mg/200ml, 25mg/200ml, 50mg/200ml and 100mg/200ml. After each sonication process, the dispersion appeared to be milkier as the concentration was increased. The penetration of the source emission was measured for each concentration using an Ocean Optics Spectrometer.

3.6.2 Optimization Experiment II

This experiment was based on the hypothesis that the type of dispersion and agitation state can affect the degree of charge separation when the material interacts with light. As shown in Figure 3.8, they are three types of dispersions: solution, colloid and suspension dispersions.

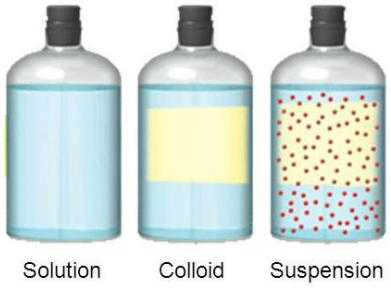

Figure 3.8 - Types of dispersions

For the experiment, only the colloid and suspension types of dispersions with the same material concentration were evaluated. The colloid was achieved after a 7-day non-stop stirring period. The suspensions were further divided into 3 groups based on the agitation state they were under during the photocatalytic process. These groups were named Stir, NoStir and Sonicate. Their names referred to the states of agitation that they were subjected to.

Chapter 4 - Results and Discussion

4.1 Material Characterization Results

4.1.1 Graphitic Carbon Nitride (g-C_3N_4)

4.1.1.1 Structure and Morphology

4.1.1.1.1 X-ray Diffraction

The phase structure of the samples is represented by the XRD diffraction patterns displayed in Figure 4.1. In both samples, UCN and TCN, the peak of highest intensity, indexed as (002), is observed at 2θ = 27.24°. It is attributed to the interlayer stacking of conjugated aromatic systems. It corresponds to an interplanar distance of 3.27 Å, obtained using Bragg's law. This strong peak represents a heptazine-based phase of g-C_3N_4 [76].The other pronounced peak indexed as (100) is of lower intensity and is found at 2θ = 13.23°.

It is characteristic of the in-plane structural packing of aromatic systems with an average void-to-void distance of 6.69 Å. These peak positions are consistent with those presented in the literature for g-C_3N_4. The crystallite sizes estimated by the Scherrer equation are ~7.8 and ~5.9 Å for TCN and UCN, respectively. Since smaller crystallite sizes generally make smaller particle sizes, UCN is expected to have a higher total surface area which could be favorable to photocatalysis [22].

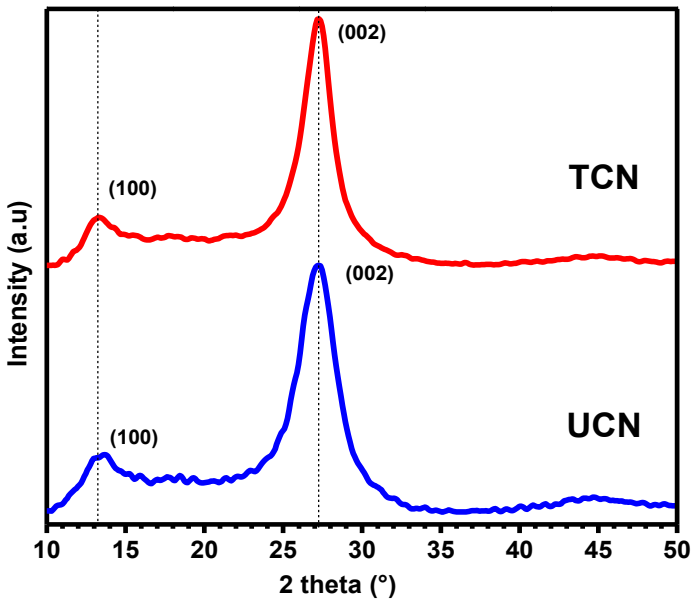

Figure 4.1 - X-ray diffraction patterns of UCN and TCN

4.1.1.1.2 Raman Spectroscopy

The molecular vibrations of TCN and UCN were examined by Raman Spectroscopy and their corresponding results are illustrated in Figure 4.2. Several characteristic peaks of g-C_3N_4 can be observed at 478, 707, 752, 977, and 1233 cm^{-1}. The ratio I_{752}/I_{707} compares the peak intensity of the band at 752 cm^{-1} to the peak at 707 cm^{-1} and corresponds to the layer-layer deformation vibrations induced by layer-layer vibrations [77].

According to these Raman spectra peaks (see Figure 4.2) I_{752}/I_{707} (TCN) < I_{752}/I_{707} (UCN); which means that UCN presents more layer-layer deformation vibrations than TCN. This difference can be further evaluated from the analysis of morphology. It is known to occur as a result of the distinct formation mechanisms of the precursors based on their chemical structures [78,79]. The bands between 800 cm^{-1} and 1000 cm^{-1} are assigned to the breathing modes of triazine rings [80,81] while the band at 1233 cm^{-1} is attributed to stretching vibration modes of C=N and C-N heterocycles [82].

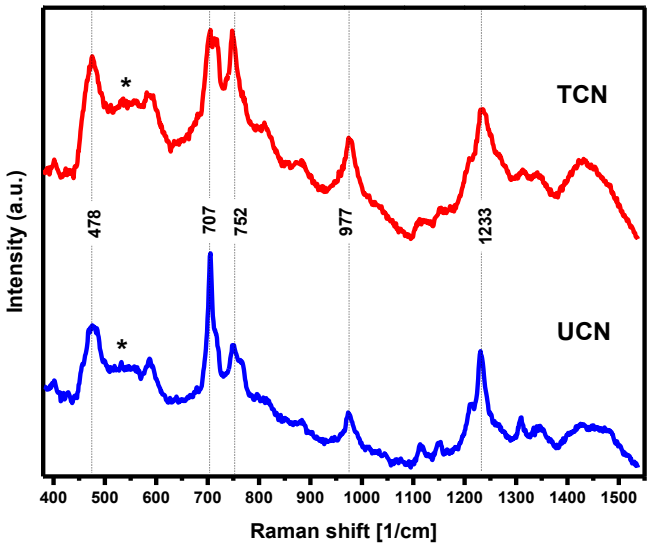

Figure 4.2 - Raman Spectra of TCN and UCN

4.1.1.1.3 FTIR Spectroscopy

The FTIR spectra of TCN and UCN are shown in Figure 3. The band at 810 cm^{-1} is attributed to the bending of triazine units. The multiple bands from 1236 to 1639 cm^{-1} are characteristic of stretching vibrations of C-N heterocycles. The peak observed at 2177 cm^{-1} corresponds to asymmetric stretching vibrations of cyano groups (−C≡N). The bands in the range 3200 to 3400 cm^{-1} are owed to terminal amino groups (−NH and $-NH_2$) which is characteristic of carbon nitrides that achieve higher degrees of condensation during synthesis [34,83,84]. Therefore, the intensity of the latter band suggests that TCN reached a higher degree of condensation than UCN. This is congruent with the yield percentages (25 % for TCN and 7 % for UCN) calculated after the synthesis processes for each material.

During synthesis, material decomposition and condensation are competitive processes dependent on the number of impurities present during pyrolysis [85,86]. The higher yield percentage from the preparation of TCN suggests that it had fewer impurities and therefore achieved a higher degree of condensation.

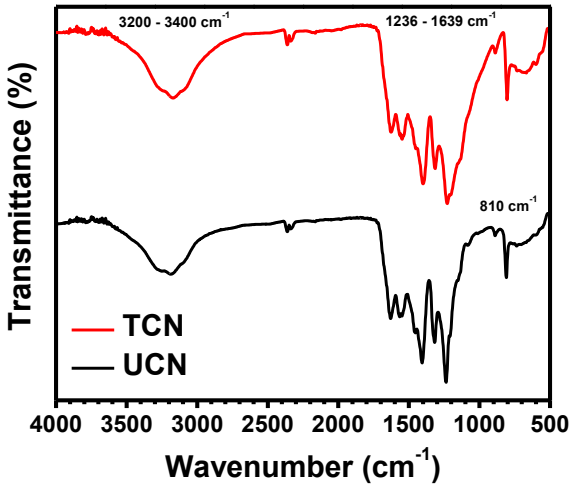

Figure 4.3 - FTIR Spectra of TCN and UCN

4.1.1.1.4 BET analysis

Brunauer–Emmett–Teller (BET) specific surface area results show that UCN has a surface area of 60.1 m^2/g and TCN has a surface area of 7.7 m^2/g. This suggests that TCN may consist of larger particles than those of UCN as shown in literature. The surface area of a gram of UCN is about 7 times larger than that of TCN. These results are also congruent with the crystallite sizes obtained from the Scherrer equation.

The higher total surface area can be attributed to an increase of porosity in UCN [24]. The benefit of having photocatalysts with large specific surface areas is their increased adsorption capacity. During a hydrogen evolution reaction (HER) these catalysts adsorb many water molecules. This increases the photocatalytic interactions and hence the efficiency of water splitting at the surface of the photocatalyst.

4.1.1.1.5 Electron Dispersive Spectroscopy

The Energy Dispersive Spectroscopy (EDS) results TCN are shown in Figure 4.4 and Figure 4.5 whilst those for UCN are shown in Figure 4.6 and Figure 4.7. The percentage content of the carbon and nitrogen elements as well as their distribution are estimated from the EDS spectra and mappings in the sites shown. A silicon substrate was used during the experiments. hence its corresponding peak is also observed. With silicon being the substrate, the background in silicon mappings should be bright unless different material is on the silicon substrate; and depending on the density of the deposited material on silicon, the

background silicon signal might be reduced or even eliminated when the material on silicon is too dense or thick.

The mapping of silicon under TCN is darker than the mapping of silicon under UCN. This suggests that there may be a very dense packing of particles, possibly due to stronger agglomeration in TCN than in UCN. Furthermore, the average atomic fractional ratios C/N in TCN and UCN were found to be 0.54 and 0.55, respectively as summarized in Table 4.1. Compared to the stoichiometric fractional ratio C/N in C_3N_4 of 0.64, these ratios indicate that both TCN and UCN have carbon deficiencies owing to C/N steam reforming reactions: $CN+NH_3>HCN+H_2$ and $C+HN_3>N_2+CH_4$ [39,83]. These deficiencies form carbon vacancies. The presence of carbon vacancies may induce acceptor states that lead to the establishment of p-type behavior.

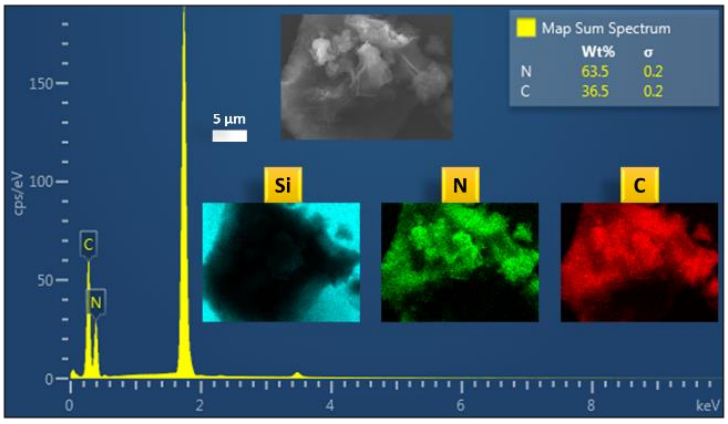

Figure 4.4 - EDS with SEM image and EDS mappings of TCN (site 1/2)

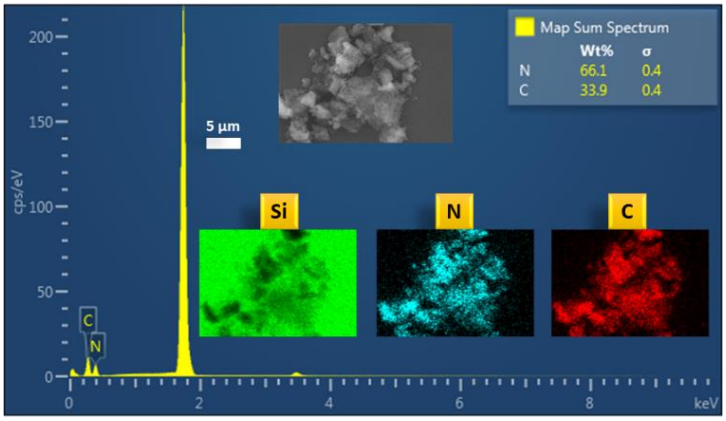

Figure 4.5 - EDS with SEM image and EDS mappings of TCN (site 2/2)

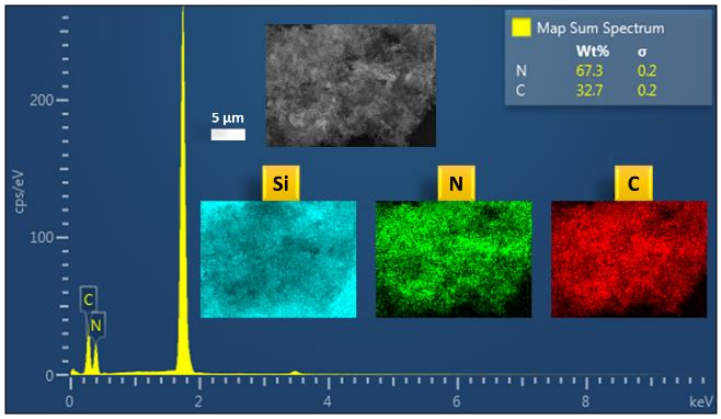

Figure 4.6 - EDS with SEM image and EDS mappings of UCN (site 1/2)

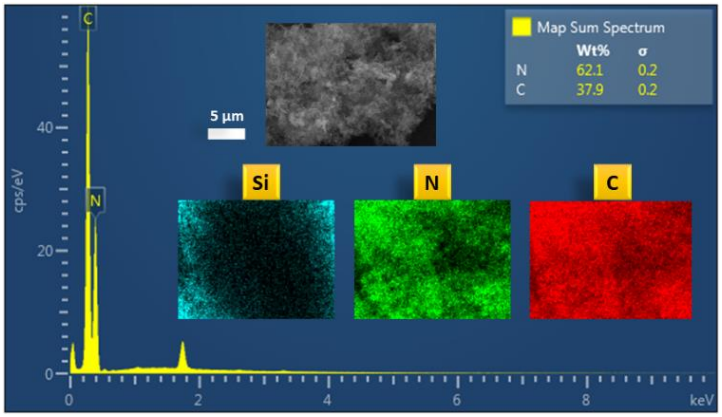

Figure 4.7 - EDS with SEM image and EDS mappings of UCN (site 2/2)

Table 4.1 - Summary of atomic proportions in TCN and UCN

EDS samples	C	N	C/N	average	Stoichiometric C/N in g-C_3N_4
TCN1	36.5	63.5	0.57	0.54	0.64
TCN2	33.9	66.1	0.51		
UCN1	32.7	67.3	0.49	0.55	
UCN2	37.9	62.1	0.61		

4.1.1.1.6 Scanning Electron Microscopy

The morphologies of UCN and TCN were observed by Scanning Electron Microscopy (SEM). In the Figure 3(a), TCN is comprised of aggregated microstructure sheets. A predominant laminar morphology which is congruent with TCN's higher crystallinity can be observed. Along the boundaries of the sheets, the surfaces are rough with fracture domains that reveal facets and contour lines.

The SEM image of UCN is shown in Figure 3(b). Its representation is similar to wrinkled sheets with a very high overall porosity[87,88]. The sheets have edges of approximately 20 nm and spread over grains with an average size of 10μm. The wrinkle morphology type of UCN is congruent with, and is a result of, its higher degree of layer to layer deformation vibrations. The porosity of the particles and thinness of their layers is an advantage to the photocatalytic efficiency because it implies that they have a larger surface area which increases the number of active facets [89].

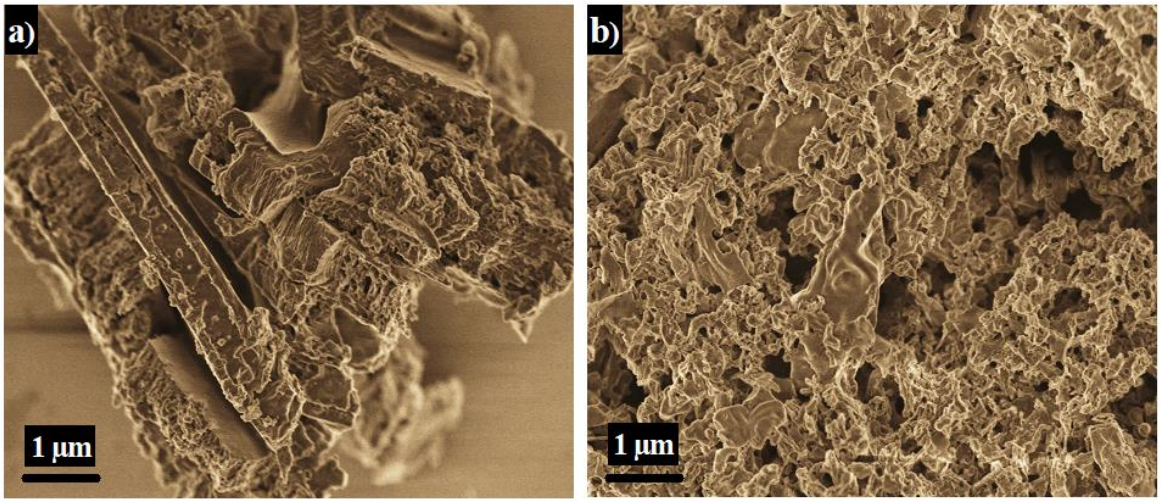

Figure 4.8 - Scanning Electron Microscope Images of a) TCN and b) UCN

4.1.1.2 Photoluminescence and Electronic Properties

4.1.1.2.1 Absorption Properties

The UV-vis absorption spectra for TCN and UCN are shown in Figure 4.9. The absorption range of TCN is very broad with an absorption edge of about 593 nm, whereas UCN has its absorption edge at 450 nm. This suggests that TCN has an improved light harnessing capacity for a wider range of visible light than UCN and this is favorable for visible-light-driven photocatalytic processes.

The extension of the bandgap edge in g-C_3N_4 has been owed to the introduction of structural defects such as cyano group (−C≡N) and is characteristic of g-C_3N_4 with high degrees of condensation[90]. This could also be a consequence of the higher rate of dissociation of Sulfur-Hydrogen (S−H) bonds during the calcination of thiourea since Sulfur induces an acceleration to the polymerization chemical process[22]. The S−H dissociation is both kinetically and thermodynamically favorable over Oxygen-Hydrogen (O−H) dissociation[91].

According to the Tauc plot slope fitting and is shown in the inset of Figure 4.9, TCN has a bandgap of 2.7 eV and UCN has a bandgap of 2.9 eV. TCN has a smaller bandgap than UCN as expected from their absorption properties. These values correspond to the minimum energies necessary for direct allowed transitions of electrons from the valence band to the conduction band when excited by a photon. The smaller bandgap of TCN compared to that of UCN has been reported as characteristic of carbon nitrides that achieve high degrees of condensation[92,93]. The advantage of a small bandgap is the reduction in the H_2 evolution activation barrier which leads to improved visible light energy harvesting.

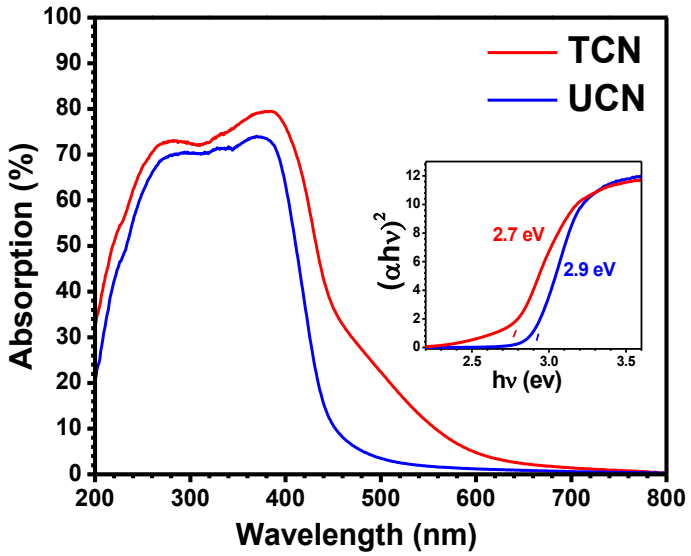

Figure 4.9 - Absorption spectra and Tauc plot (inset) of TCN and UCN

4.1.1.2.2 Electronic Properties

Apart from the band gap size, the band gap position is critical to the performance of semiconductor photocatalysts. Mott Schottky plots of TCN and UCN and their estimated flatband potentials are shown in Figure 5. It was revealed that both TCN and UCN have both n-type and p-type semiconductor conductivity behavior hence form p-n homojunctions. The p-type behavior is attributed to the presence or carbon vacancies which increase the acceptor concentration[94]. Upon extrapolating the regions of linearity, their estimated flatband potentials were 2.71 V and 1.51 V for TCN and UCN, respectively. With these values it was possible to calculate the electrochemical potential of the valence bands.

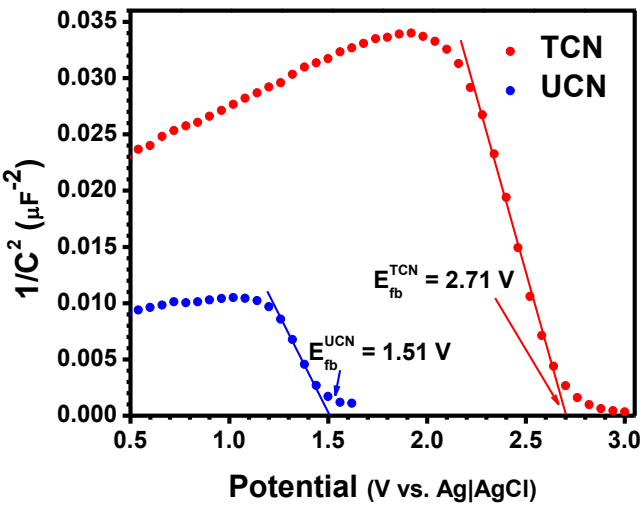

Figure 4.10 - Mott Schottky plots of TCN and UCN

Furthermore, the charge carrier density can be calculated from the slope of the plot since the carrier density of the electrode material is inversely proportional to the slope of the plot according to the equation [95]:

$$N_Q = \frac{2}{\varepsilon\varepsilon_0 e}\left[\frac{d\left(\frac{1}{C^2}\right)}{dV}\right]^{-1} \quad (6)$$

where ε denotes the dielectric constant of the material, ε_0 is the permittivity of the vacuum (8.854×10^{-12} Fm^{-1}), the factor e is the electronic charge unit, i.e. 1.602×10^{-19} C, and V is the potential applied at the electrode. According to equation 6, both the positive and negative slopes of UCN are smaller than the slopes of TCN which means that the donor and acceptor densities of UCN are higher than those of TCN. This is congruent with the higher quantity of amino groups in TCN which function as recombination centers. This is because the quantity of recombination sites is inversely proportional to the charge density[84].

The arc radius of an EIS Nyquist plot indicates the effectiveness of the separation of photo-generated electron–hole pairs and the rate of the interfacial charge transfer process [96]. The Nyquist plot of TCN and UCN obtained under visible light is represented in Figure 4.11. It can be observed that the arc radius in the plot of UCN is smaller. This implies that UCN has a higher charge carrier separation and transfer efficiency than TCN. This property is attributed to the presence of a higher electric field and to band gap alignment in UCN [96].

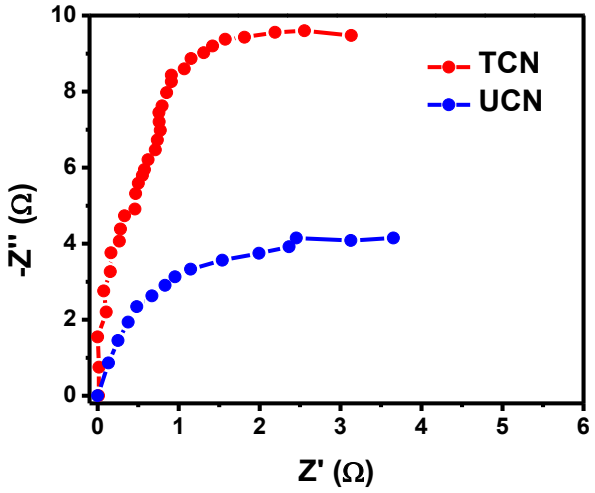

Figure 4.11 - Nyquist plots of TCN and UCN

The bandgap positions for TCN and UCN are illustrated in Figure 4.12 with reference to the Normal Hydrogen Electrode (NHE) scale. The position defines the strength of the materials to carry out redox reactions. Normally, materials with high reduction strengths work best as photocatalyst for hydrogen generation whilst those with high oxidation strengths work best as photocatalysts in the degradation of chemical compounds [97]. Figure 4.12 presents band edge positions of the synthesized materials. It shows that TCN and UCN have different band gap positions.

UCN has its conduction band positioned higher than that of TCN with respect to the water splitting reduction limit (H^+/H_2) of the NHE scale. This means that UCN has a greater reduction power than TCN. On the other hand, TCN has its valence band positioned lower than that of UCN with respect to the water splitting oxidation limit (O_2/H_2O) of the NHE scale. This means that UCN has a greater oxidation power than TCN. Both materials have their bandgap edges overlapping the water splitting limits which affirms them as candidate photocatalysts for hydrogen evolution.

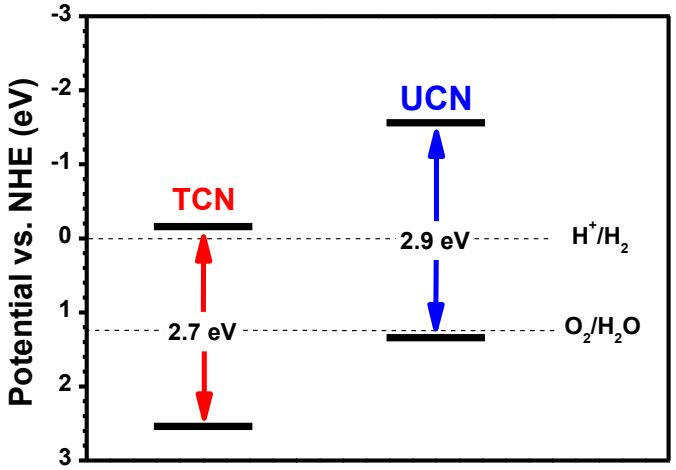

Figure 4.12 - Band gap Positions of TCN and UCN

4.1.1.2.3 Photoluminiscence

Figure 4.13 shows the PL emission spectra of TCN and UCN when excited at wavelengths: 254 nm (UV), 405 nm (violet-blue) and 440 nm (blue). When excited by UV light both photocatalysts showed the lowest overall emission intensities with their main peaks at 360 nm. Upon excitation by visible light, their emission intensities were dependent on the wavelength of the source (either 405 nm or 440nm). First, when excited with violet-blue light at 405 nm, TCN has a lower emission intensity than UCN with their main emission peaks centered around 467 nm.

A similar emission range has been reported for various types of g-C_3N_4 under the excitation of UVA irradiation (380 nm) wherein decreased fluorescence emission in this range is attributed to defect structures which introduce localized energy levels inside the band gap hence forming recombination centers[84,98]. On the other hand, when excited with blue light their main emission peaks are centered at 500 nm. TCN has a higher emission intensity than UCN. Therefore, the fluorescence properties of TCN and UCN are strongly dependent on the wavelengths of excitation.

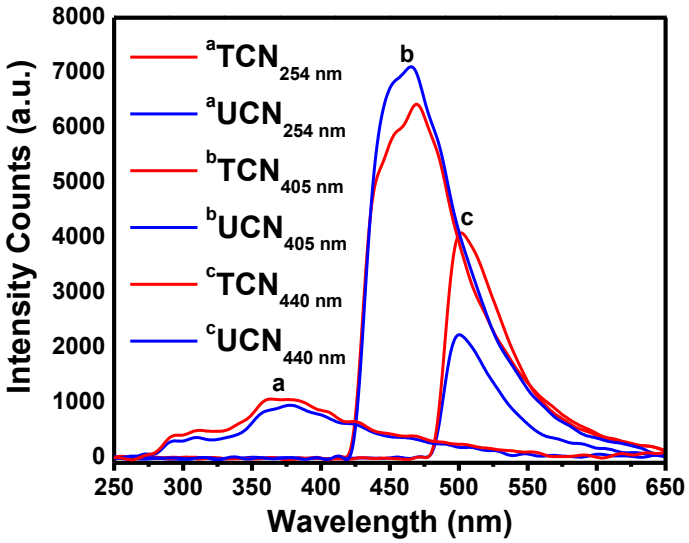

Figure 4.13 - Emission Spectra of TCN and UCN under UV and visible light excitation

4.1.2 Alkaline Metal Aluminates ($BaAl_2O_4$ and $MgAl_2O_4$)

4.1.2.1 Structure and Morphology

4.1.2.1.1 X-ray Diffraction

Figure 4.14 shows the X-ray diffraction patterns of the carbon or air annealed barium aluminates conforming to the standard $BaAl_2O_4$ pattern (ICDD 01-73-0202). The diffraction peaks can be readily indexed as hexagonal $BaAl_2O_4$. The ratios of the main peak intensities to that of their adjacent peaks ($\delta = I_{main}/I_{adj}$) leads to the comparison of the degree of crystallization between the materials [99]. The superiority of this ratio for the BAC pattern compared to that of the BCC pattern is an indication of a higher crystallinity for BAC. This difference is a consequence of the thermal treatment atmosphere.

It is supposed that thermal treatment with carbon powders presents a reductive atmosphere that may lead to a deficiency of oxygen atoms from the unit cells of $BaAl_2O_4$ [100,101]. It is suggested that the increase in the density of this defect type may result in the destabilization of the overall structural order of the crystal lattices hence the low crystallinity in BCC. The average crystallite sizes were approximated using the Scherrer equation from which the average crystallite size of BCC was 96 nm while that of BAC was 113 nm.

Figure 4.15 shows a similar comparison between the X-ray diffraction patterns of carbon or air annealed magnesium aluminates. The patterns conform to the standard $MgAl_2O_4$ pattern (ICDD 01-73-6383) and their peaks can be indexed as cubic $MgAl_2O_4$. By comparing the ratio of the intensities of the main peaks to their adjacent peaks, it is observed that δ_{MCC} is

superior to δ_{MAC}. This implies improved crystallization in MCC and suggests that carbon annealing can enhance the crystallinity of magnesium aluminate. This advantage can be owed to the higher surface-to-volume ratio of the magnesium aluminate crystals that favors their maneuverability and phase equalization amidst induced oxygen vacancy defects [102,103]. The average crystallite sizes were approximated as 80 nm for MCC and 60 nm for MAC.

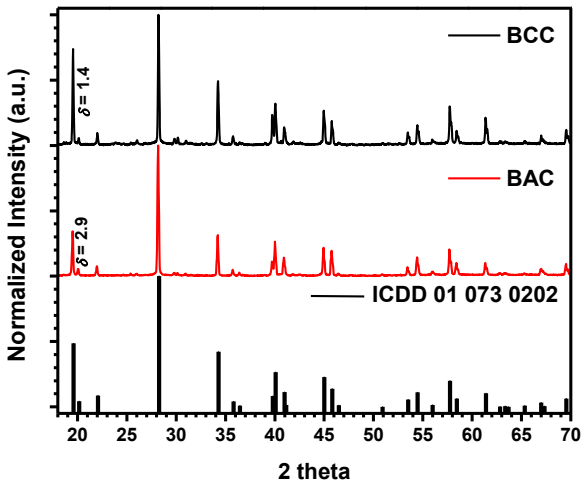

Figure 4.14 - X-ray diffraction patterns of barium aluminates

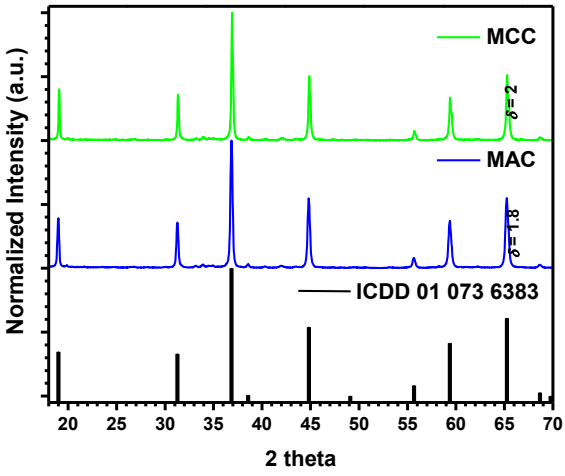

Figure 4.15 - X-ray diffraction patterns of magnesium aluminates

4.1.2.1.2 Scanning Electron Microscopy

SEM micrographs of the materials are shown in Figure 4.16. The microstructures of the $BaAl_2O_4$ as shown in Figure 4.16 a) and Figure 4.16 b) crystallized to form agglomerated irregular clusters of about 0.5 μm. Long and sharp ends can also be identified. These may

have been formed from the growth of twinned hexagonal-phase crystal edges. The application of a specific thermal treatment atmosphere does not seem to carry any significant modification to the morphology of the $BaAl_2O_4$.

On the other hand, smaller pebble-like particles are observed in the images of the $MgAl_2O_4$ materials Figure 4.16 c) and Figure 4.16 d). These particles exhibit a high packing density and a nucleated distribution. Flat surfaces can be identified and may be attributed to the growth of twinned cubic-phase crystal surfaces. Single particle sizes observed from the SEM images are within the order of the approximated crystallite sizes and range between 0.05 μm to 0.15 μm. Smaller particles with the least agglomeration are favorable to photocatalytic processes as they favor increased interactions of their surfaces with photons, molecules and various ionic species.

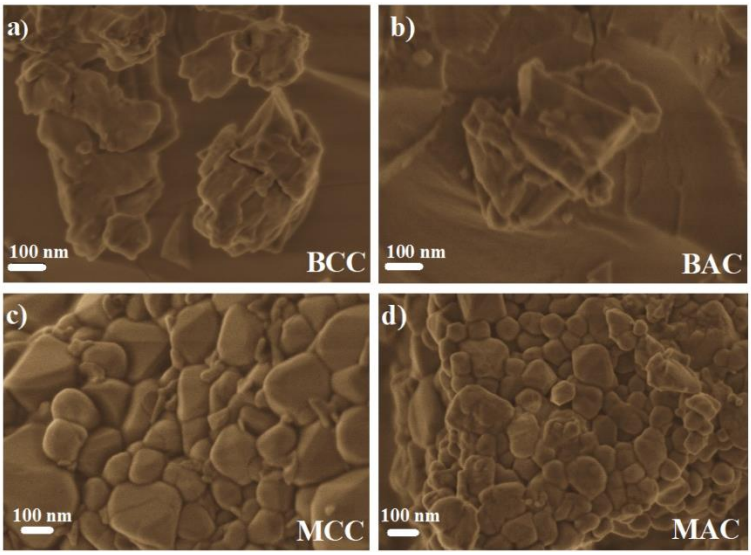

Figure 4.16 - Scanning electron microscopy of alkaline metal aluminates

4.1.2.2 Photoluminescence and Electronic Properties

4.1.2.2.1 Absorption Properties

Absorption spectra of the samples are presented in Figure 4.17. The BAC sample uniquely portrays the highest absorption property followed by BCC, MAC and finally MCC, in the UV spectral region. In either aluminate type, carbon annealed samples have inferior absorption bands. In general, it is expected that reductive heat treatment atmospheres will lead to the generation of surface oxygen vacancies that act as electron trap sites which in turn might result in stronger absorption bands. However, prolonged reduction may form bulk oxygen vacancies which consequently lower the charge separation efficiency because they act as charge carrier recombination sites.

The inferiority of the absorption bands of the reduced aluminates presented in this work may be due to the formation of more bulk oxygen vacancies than surface oxygen vacancies [104,105]. Tauc plots of each material are shown in the inset in Figure 4.17. Assuming all samples as direct electronic transition semiconductors the band gaps of the materials were approximated. The $BaAl_2O_4$s had slightly narrower band gaps of 3.74 eV and 3.88 eV for BCC and BAC, respectively. The $MgAl_2O_4$s had the widest bandgaps of 4.18 eV and 4.09 eV for MCC and MAC, respectively. The reduction in the band gap value is in agreement with the increase of the average crystallite size, as estimated by Scherrer equation, of the nanomaterials [106].

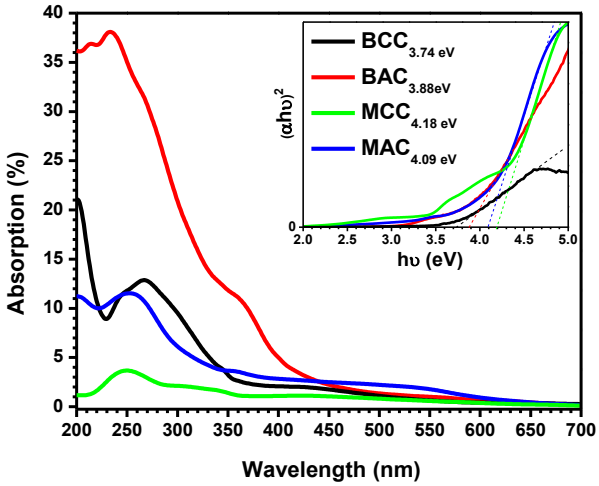

Figure 4.17 - Absorption spectra of alkaline metal composites

4.1.2.2.2 Electronic Properties

To better understand redox behavior of the materials for photocatalytic processes, their electrochemical potentials with respect to the Normal Hydrogen Electrode (NHE) were determined and are shown in Figure 4.18. The conduction bands of all the samples have almost the same negative electrochemical potential which means that photogenerated electrons in these bands may possess comparable reducing power. The valence bands of the Magnesium Aluminates have the highest positive electrochemical potential of all the synthesized materials. This means that photogenerated holes in these bands are most likely to have greater oxidizing power than the Barium Aluminates.

As a correlation to these measurements, the obtained Mott Schottky plots clearly characterize the $BaAl_2O_4$ samples as a n-type material and the $MgAl_2O_4$ samples as p-type materials. All the $MgAl_2O_4$ samples have their band edges completely enveloping the water stability limits (0 eV and 1.23 eV). This suggests them as candidate photocatalysts for water splitting applications. The $BaAl_2O_4$ samples on the other hand have their valence

band edge potentials only a little below the water oxidation limit of 1.23 eV. This therefore does not undermine their power to perform oxidation reactions as well.

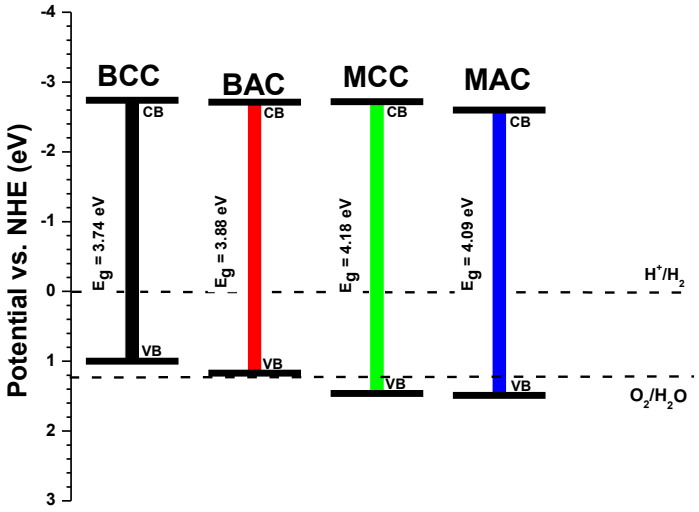

Figure 4.18 - Electrochemical potentials of alkaline metal aluminates

4.1.2.2.3 Photoluminescence

The emission spectra, shown in Figure 4.19, correspond to UVC wavelength excitation with broad principal visible emissions centered at 423 nm for $MgAl_2O_4$ samples and at 533 nm for $BaAl_2O_4$ samples. Oxygen vacancies and F-centers form shallow-trap and deep-trap states from which the observed broad band emissions originate [107]. Upon UVC excitation, the F-centers undergo photoconversion. This process promotes the electrons to the conduction band and the trap sites. The electrons in the conduction band can fall into the trap sites. The relaxation of the excited electrons from the shallow-trap sites results in rapid and narrower emissions.

On the other hand, the relaxation of the excited electrons from the deep-trap sites results broad and persistent emissions [108]. By integrating the emission spectra within the presented limits (400 nm and 640 nm) it was found that BAC represents an emission density reduction of 78% with respect to BCC whilst MCC represents an emission density reduction of 8 % with respect to MAC. Interestingly the most crystalline samples of each material type present the lowest emission density. Since the emission density is proportional to the charge (electron-hole pair) recombination density, BAC and MCC each have the lowest charge recombination densities. To have good photocatalytic activity there must be high population inversion and low charge recombination [109].

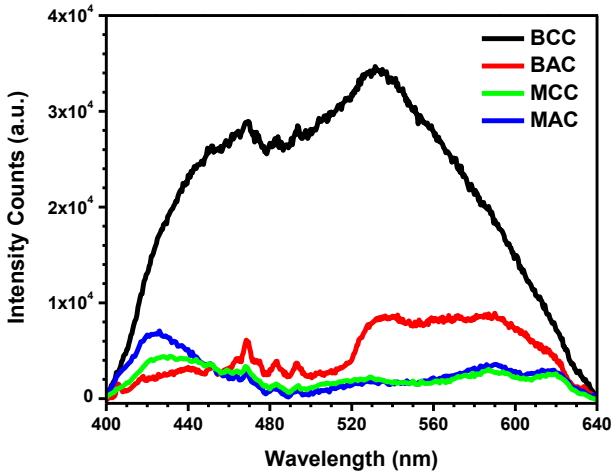

Figure 4.19 - Emission properties of alkaline metal aluminates

4.2 Experimental Results

4.2.1 Photocatalytic hydrogen generation using g-C_3N_4 p-n homojunction under UV and visible light

4.2.1.1 Optimization Experiment I

4.2.1.1.1 Analysis of Light Transmission through within Reactor

Figure 4.20 shows different transmission intensities of light from a 405 nm LED strip source illuminating through dispersions with varying densities. The mass of graphitic carbon nitride prepared from urea (UCN) is the variable on which the dispersion density depends. A high transmission intensity corresponds to a higher light penetration efficiency whereas a low transmission intensity suggests a lower penetration efficiency. The transmission intensities are inversely proportional to the mass of photocatalyst constituting each dispersion.

The results suggest that the highest light penetration efficiency occurs when only 1 mg of UCN is added to the aqueous solution. Any amount beyond 100 mg is prone to very low light penetration if any at all. Between these extremes, half the maximum (50 %) observed intensity corresponds to adding only 5 mg of photocatalyst. These results are an indication of the degree of interaction between photocatalyst particles and photons. A 50 % transmission intensity with respect to the observed intensity extremes may mean that 5 mg of this photocatalyst is ideal for the photocatalysis experiment. This is because it indicates that the dispersion density is not so high that it limits light exposure only to the particles

that are nearest to the source. The dispersion density is neither too low that it renders most of the generated photons as wasted.

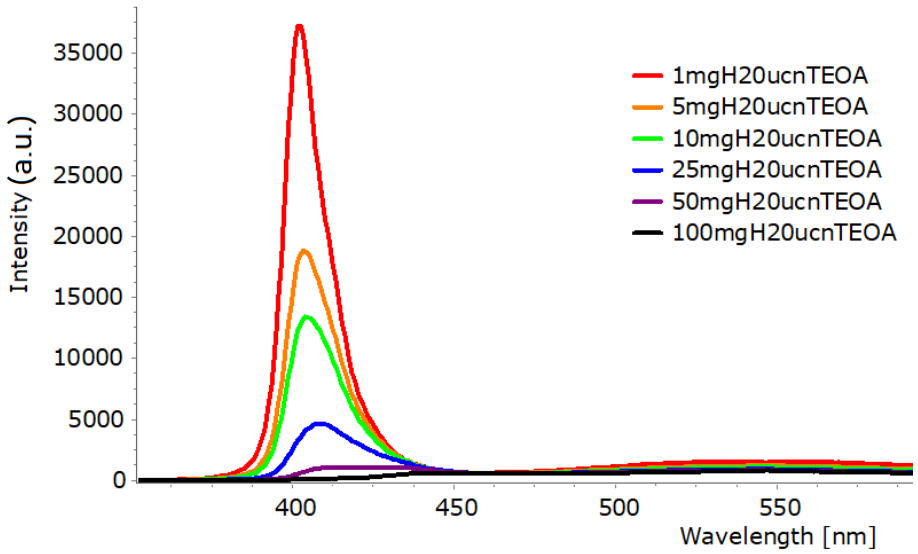

Figure 4.20 - Measured transmission Spectra through reactor

4.2.1.2 Hydrogen Evolution

The rates of hydrogen production using TCN and UCN as photocatalysts under UV (254 nm) and visible light (405 nm and 440 nm), are presented in Figure 4.21. On the overall, TCN performs best under UV light whilst UCN performs best under visible light.

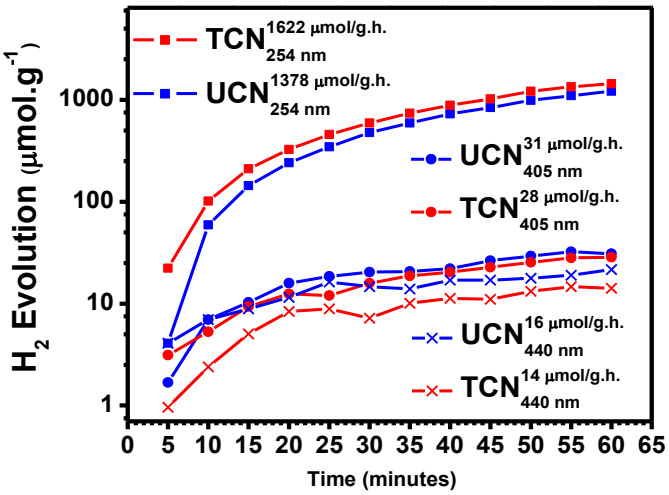

Figure 4.21 – Hydrogen Evolution Rates of TCN and UCN under UV and visible light

4.2.1.3 Efficiency

To quantify and compare the performance of each photocatalyst under varied irradiation sources the apparent quantum yield was calculated according to the following equation [75]:

$$AQE\% = \frac{2 \times number\ of\ evolved\ H_2\ molecules}{number\ of\ incident\ photons} \times 100 \quad (4)$$

or

$$AQE\% = \left(\frac{2 \times \beta \times N \times c \times h}{I \times S \times t \times \lambda \times 2\pi}\right) \times 100 \quad (5)$$

where β is the quantity of evolved hydrogen (mol), N is Avogadro's number, c is the speed of light ($m.s^{-1}$), h is Planck's constant (Js), I is the irradiance of the source (W/cm^2), S is the surface area illuminated by the source (cm^2), t is the time of the reaction process (s) and λ is the wavelength of the illumination source (m).

Table 4.2 summarizes the hydrogen generation rates and efficiencies (calculated according to equations 4 and 5) achieved under the varied sources. The highest hydrogen evolution rate of 1622 $\mu mol.g^{-1}.h^{-1}$ corresponding to an AQY of 3.2% was obtained using TCN.

Table 4.2 – Hydrogen Generation Rates and Efficiencies with various sources

Sample	254 nm Irradiation wavelength		405 nm Irradiation wavelength		440 nm Irradiation wavelength	
	Evolved H_2 ($\mu mol.g^{-1}.h^{-1}$)	AQY (%)	Evolved H_2 ($\mu mol.g^{-1}.h^{-1}$)	AQY (%)	Evolved H_2 ($\mu mol.g^{-1}.h^{-1}$)	AQY (%)
TCN	1622	3.2	28	1.5	14	0.1
UCN	1378	2.8	31	1.6	16	0.1

Upon analysis with reference to Figure 8, it is proposed that excitation with UVC irradiation (254 nm) causes the emission of violet UVA irradiation (at 360 nm by radiative decay) which re-excites the photocatalyst. Such a re-excitation process favors the photocatalytic performance of TCN over UCN because the carrier charge recombination in TCN is suppressed under violet-blue excitation.

Following the latter proposal, it is also expected that an excitation with violet-blue UVA irradiation (405 nm) emits blue light (at 467 nm by radiative decay) which re-excites the photocatalyst. This process favors the photocatalytic performance of UCN over TCN because the carrier charge recombination in UCN is suppressed under blue light excitation.

Finally, when the materials are under the direct excitation of blue light (at 440 nm) UCN still performs better than TCN similarly due to a higher suppression of carrier charge

recombination. Considering the band gap size, the radiative emission near green light (500 nm) caused by blue light excitation represents very low energy for the re-excitation phenomenon to be repeated.

4.2.2 MAl_2O_4 (M= Ba, Mg) photocatalytic activity dependence on annealing atmosphere

4.2.2.1 Optimization Experiment II

4.2.2.1.1 Variation of light-photocatalyst interaction conditions for hydrogen generation by $MgAl_2O_4$

The hydrogen generation rates obtained with $MgAl_2O_4$ in four different dispersion presentations are shown in Figure 4.22. Each dispersion represents a unique light photocatalyst interaction condition. According to the results, the No-Stir-Colloid is the best condition for the generation of the highest quantities of hydrogen using $MgAl_2O_4$ It is closely followed by the Sonicate condition, then the Stir condition and finally the No-Stir-condition. This means that it is better to stir a dispersion continuously during a photocatalysis reaction than not to stir it at all.

Furthermore, it is better to constantly sonicate the dispersion whilst carrying out a photocatalysis reaction than to stir it. Finally, it is best to prepare a colloidal dispersion for photocatalysis reaction than to use a non-colloidal dispersion. This condition proves so effective that no stirring is required to achieve enhanced results.

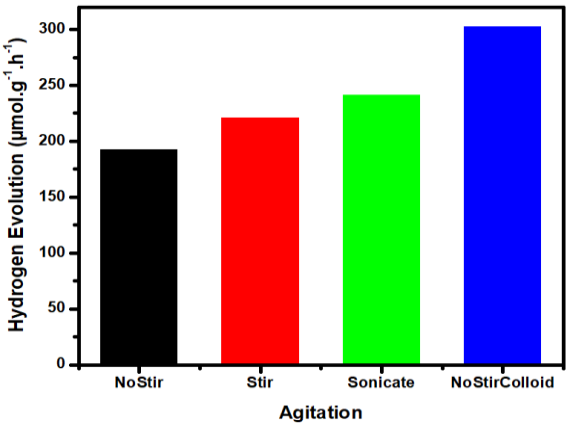

Figure 4.22 - Hydrogen generation rates at varied interaction conditions using MgAl2O4

4.2.2.2 Dye Degradation

Each of the material's dye degradation experiment results follows a unique degradation rate path as shown in Figure 4.23. The reference sample, MB solution without any catalyst, underwent degradation by photolysis and achieved a degradation percentage of only 36 %, while BAC achieved complete degradation after 90 minutes. The $BaAl_2O_4$ samples perform as better photocatalysts for MB dye degradation which is an oxidation dependent reaction. This could owe to their smaller bandgap which allowed the material to respond effectively to the broad irradiation spectrum of solar simulated light energy.

The other advantage of $BaAl_2O_4$ samples over the $MgAl_2O_4$ samples is their higher absorption capacities which lead to a higher population inversion density. Based on the emission properties it is as expected for BAC to perform better than BCC. In the case of the Magnesium Aluminates, the MAC sample performs better than MCC sample. On the overall, it appears that the air annealed samples of each material type work more effectively as photocatalysts for the MB dye degradation experiments.

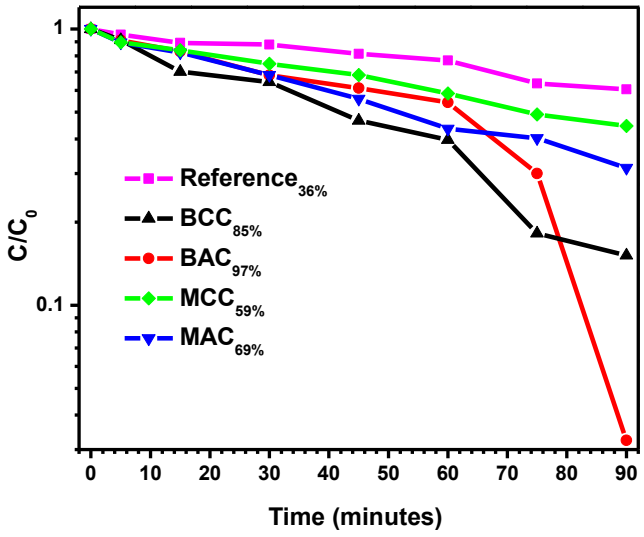

Figure 4.23 – Dye degradation profiles of Alkaline Spinel Aluminates

4.2.2.3 Hydrogen Generation

The hydrogen generation rate results, using each photocatalyst sample, are presented in Figure 4.24. It is interesting to note that between the $BaAl_2O_4$ sample materials, BCC performs better than BAC; which is contrary to the outcome from the dye degradation experiments. A rate of 86 $\mu mol.h^{-1}.g^{-1}$ is achieved with BCC whereas 75 $\mu mol.h^{-1}.g^{-1}$ is achieved by using BAC.

Similarly, between the $MgAl_2O_4$ samples, MCC performs better than MAC which is also contrary to the outcome from the dye degradation experiments. MCC achieves the highest rate of 97 $\mu mol.h^{-1}.g^{-1}$ while MAC achieves a 64 $\mu mol.h^{-1}.g^{-1}$rate. Thus, on the overall, Carbon annealing appears to enhance the performance of either material for photocatalytic hydrogen generation, which is majorly a reduction dependent reaction. This is a promising result for material design.

The highest H_2 evolution rate is attributed to surface oxygen vacancies that function as electron trap sites and allow electrons to quickly interact with hydrogen cations in producing hydrogen. In addition, the wideband gap of MCC across the water stability limits theoretically renders it enough redox power to split the water molecule whilst reducing hydrogen cations.

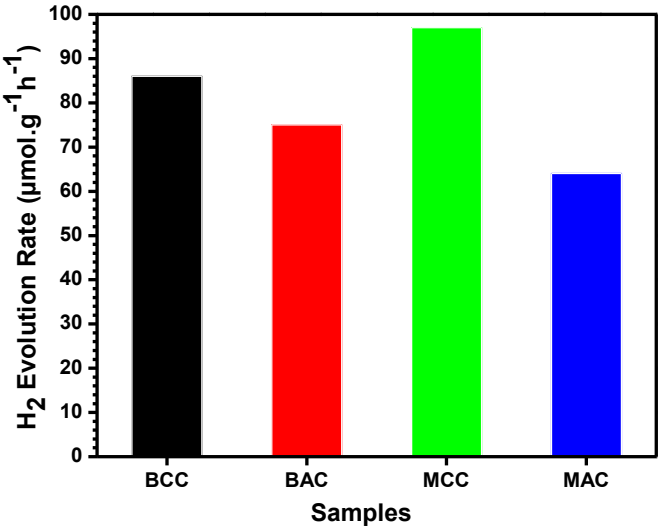

Figure 4.24 – Hydrogen Evolution Rates using Alkaline Metal Aluminates

Chapter 5 - Conclusions

5.1 Two-dimensional Materials

Graphitic carbon nitride p-n homojunctions were successfully obtained from a 3-hour direct heat calcination synthesis process of urea or thiourea at 550°C. The photocatalysts achieved the same phase structures but distinct morphology, optical and electronic properties. UCN was composed of wrinkled and porous nanosheets while TCN was made up of straight and stacked nanosheets. The formation of the p-n homojunction resulted in stronger internal electric fields which were responsible for the enhancement of the charge separation and transport efficiency especially in UCN.

The estimated band gaps were 2.7eV for TCN and 2.9 eV for UCN. Their band edges overlap the water splitting energy limits. The beneficial photocatalytic attributes of UCN include its smaller particle size, higher total surface area, higher reduction capacity, higher charge density and more efficient charge separation and transfer. On the other hand, TCN achieved a higher oxidation strength, higher absorption capacity, smaller band gap and wide absorption band edge.

The photocatalytic performance of the photocatalysts is strongly dependent on the wavelength of illumination. Under UV light, both materials produced hydrogen at rates that were two orders of magnitude higher than the rates of hydrogen evolution under visible light. TCN was a slightly superior photocatalyst to UCN under UV light but inferior under visible light. The overall inferiority of the hydrogen production rates under visible as compared to UV light is mainly attributed to poor photocatalyst activation due to insufficient charge concentration which is a consequence of structural defects.

In addition, re-excitation by radiative decay emissions is suggested to play a key role in determining the final amount of available charge carriers available for the HER process. This work not only demonstrates conductivity modulation, but also contributes to the study of a unique combination of factors that affect the performance of g-C_3N_4 p-n homojunctions in hydrogen evolution reactions.

5.2 Alkaline metal aluminates

The crystallinity of barium aluminate is on the overall diminished by the carbon heat treatment atmosphere whilst that of magnesium aluminates is enhanced. The heat treatment atmosphere does not have a significant effect on the morphology nor crystallite size. It has been suggested that the absorption property of the samples is directly correlated to the ratio of the surface oxygen vacancies to the bulk oxygen vacancies.

It was observed that the absorption of either material type is diminished by carbon annealing. With reference to direct electronic transitions, the $MgAl_2O_4$ samples had the widest bandgaps with electrochemical potentials that favor water splitting whilst the

$BaAl_2O_4$ samples had narrower band gaps. Broad visible emissions under UVC excitation were observed from all the samples. The carbon annealed $BaAl_2O_4$ sample showed higher charge recombination whilst the carbon annealed $MgAl_2O_4$ sample showed lower charger recombination. The broad band visible emission spectra were ascribed to the presence of oxygen vacancies and F centers in the form of shallow and deep-trap sites.

Sample BAC was noted as the best photocatalyst for dye degradation after achieving complete photo-degradation of MB after only 90 minutes under solar simulated irradiation. This is assumed as a consequence of its high absorption capability, low electron-hole pair recombination and high valence band potential. In general, the air annealed samples favor oxidation dependent reactions such as dye degradation.

The hydrogen generation experiments revealed the MCC sample as the best photocatalyst, achieving the highest H_2 generation rate of 97 $\mu mol.h^{-1}.g^{-1}$. The advantages of MCC include its small particle size, which suggest a higher surface area for photocatalytic interactions. MCC also had the lowest density of emissions under UVC excitation owing to the generation of surface oxygen vacancies that inhibit electron-hole pair recombination.

Finally, the electrochemical potentials of the band edges of MCC are positioned around water stability limits. The overall performance of the carbon annealed photocatalysts was superior to those of the air annealed photocatalyst for the hydrogen evolution experiments, thereby suggesting that carbon annealing can enhance the photocatalytic performance of materials to be used for reduction dependent reactions.

Chapter 6 - Future Prospects

6.1 CO_2 Reduction Experiments

Photocatalytic CO_2 reduction is a mechanism in which CO_2 is converted into products such as methane, methanol, formaldehyde, formic acid and carbon monoxide in the presence of water, a photocatalyst and light irradiation. Recently, photocatalysts like zeolites, zirconium oxide, magnesium oxide, zinc oxide, zinc sulfide and graphitic carbon nitride have been evaluated for this purpose. Most of these photocatalysts are limited by factors such as UV light response exclusivity, high photogenerated charge recombination rates and low total surface areas. As such there exists a need to carry out new experiments using new or modified photocatalysts[110].

To carry out CO_2 reduction experiments, water, a photocatalyst and a light source are the principal requirements. In addition, a glass reactor, a mechanical pump, high pure-CO_2 and a gas chromatograph are required. The water should be deionized and in very small amounts to achieve water vapor (100% humidity) upon increase of pressure. The photocatalyst amount in mg may be approximately equal to or less than the amount of deionized water in µL. The light source should preferably be a 300W Xe lamp as this type is commonly used in reported work.

The results may be easier to compare with using this light irradiation source. The glass reactor should be made out of quartz in order to transmit high energy UV light frequencies. The mechanical pump should be complimented by a manometer in order to monitor the pressure generated within the reactor and secure that its regulation is within the allowed range as according to the operation specifications of the reactor. The CO2 source should have very little impurities and must have a known molarity to be considered upon calibration over the gas chromatograph whose column must be designed for the analysis of hydrocarbons[111].

6.2 Waveguide Photocatalysis Reactor

A waveguide photocatalysis reactor (WPR) is a reactor that possesses the shape of a light waveguide. In our case, as shown in Figure 6.1, a straight tubular quartz tube was used as the wave guide. The light source was placed at parallel with the tube at the closed end of the tube so that the emitted light could travel along its length.

The advantages of the WPR is include its effectiveness in reducing the amount of stray light or lost light. Almost all the light that leaves the source has a better chance of entering the reactor. Given that the reactor is a waveguide, the light is neither lost but contained within the walls of the waveguide structure. As according to the laws of reflection and refraction, the light is contained because the incident angle with which the light hits the

quartz wall (of higher refractive index) is always greater that the refractive angle with which the light rays could leave the tube towards the outside (of lower refractive index). This is the principle of total internal reflection. The other advantage of the WPR is its miniature size compared to the conventional reactor. WPRs generally have small diameters but can have greater heights to ensure that total internal reflection occurs. The miniature size allows us to use lower photocatalyst masses and therefore save on material. As such we can also use lesser quantities of aqueous media. The additional benefit because of the mentioned advantages is improved photocatalysis efficiency.

Figure 6.1 - A waveguide photocatalysis reactor

The efficiency of the photocatalytic process is improved because less light is lost due to the waveguide setup and lower irradiances are required to achieve results because less dispersion content is used in the smaller sized reactor. On the other hand, because of the smaller size and quantities of dispersion used WPR are however limited in the amount of hydrogen they can generate over long periods of time. For experimental purposes WPRs are ideal. However, for commercial purposes, multiple WPRs would have to the installed in order to harness greater amounts of hydrogen especially over long periods of reaction times.

To the best of our knowledge WPRs have not been reported as alternatives to the conventional reactor setup in which the light source is often placed from the side or around the reactor. This means that there is an opportunity of expansion when it comes to the use and optimization of WPR setups. To improve the WPR setup that was established in this work, the light sources, which were LEDs in this case could be fitted with converging lenses so as to reduce the amount of scattered light leaving the light source aperture. Further studies that can be conducted under this setup include the use of laser illumination directed toward the longitudinal end of the reactor.

6.3 Production of Diethanolamine

Diethanolamine is a member of the class of ethanolamines that is ethanolamine having a N-hydroxyethyl substitute. Diethanolamine is used in a number of consumer products, such as shampoos, cosmetics and pharmaceuticals[112]. Diethanolamine is produced by reacting ethylene oxide with ammonia. In most production facilities, ethylene oxide and ammonia are reacted in a batch process that yields a crude mixture of ethanolamine, diethanolamine and triethanolamine. The mixture is then distilled to separate and purify the individual compounds[113].

In this work we discovered that in the presence of Alkaline Aluminate photocatalysts such as $MgAl_2O_4$ or $BaAl_2O_4$, a substance with the characteristics of diethanolamine as shown in Figure 6.2, could be produced during the process of photocatalysis under UV light irradiation. This is work that is yet to be further studied. Based on our current understanding of the process of photocatalysis, it is most likely that triethanolamine, the sacrificial agent, was oxidized by the photogenerated holes whilst the photogenerated electrons reduced the hydrogen cations in the formation of hydrogen gas.

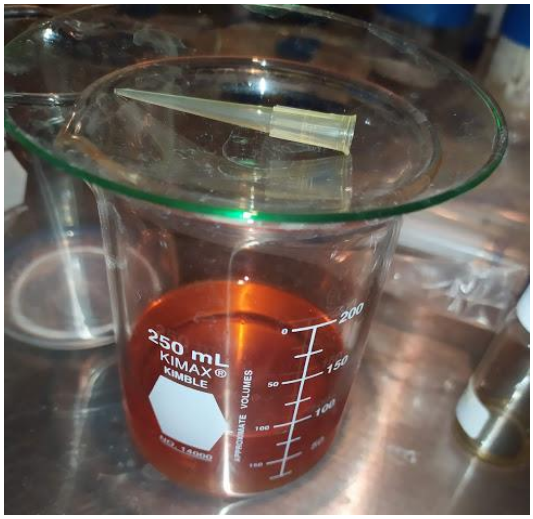

Figure 6.2 - Acquired final product of the possible diethanolamine

One way of characterizing diethanolamine is by analyzing its bond structures. This can be carried out using Raman Spectroscopy, FTIR spectroscopy or NMR spectroscopy. The advantage of using photocatalysis to produce this chemical substance is fundamentally the cost of production. There exists an opportunity to further this research and possibly the acquisition of a patent to a new method of diethanolamine manufacture.

References

1. PS, V. *et al.* Hydrogen: A sustainable fuel for future of the transport sector. *Renew. Sustain. Energy Rev.* **51**, 623–633 (2015).

2. World Energy Outlook 2016. *World Energy Outlook 2016* (2016). doi:10.1787/weo-2016-en

3. Jain, I. P. Hydrogen the fuel for 21st century. *Int. J. Hydrogen Energy* **34**, 7368–7378 (2009).

4. Edwards, P. P., Kuznetsov, V. L., David, W. I. F. & Brandon, N. P. Hydrogen and fuel cells: Towards a sustainable energy future. *Energy Policy* **36**, 4356–4362 (2008).

5. Cotterill, P. The hydrogen embrittlement of metals. *Prog. Mater. Sci.* **9**, 205–301 (1961).

6. Ramachandran, R. & Menon, R. K. An overview of industrial uses of hydrogen. *Int. J. Hydrogen Energy* **23**, 593–598 (1998).

7. Basu, P. & Basu, P. Production of Synthetic Fuels and Chemicals from Biomass. in *Biomass Gasification, Pyrolysis and Torrefaction* 415–443 (Academic Press, 2018). doi:10.1016/B978-0-12-812992-0.00012-1

8. Edwards, J. K., Freakley, S. J., Lewis, R. J., Pritchard, J. C. & Hutchings, G. J. Advances in the direct synthesis of hydrogen peroxide from hydrogen and oxygen. *Catal. Today* **248**, 3–9 (2015).

9. Brul, S. & Coote, P. Preservative agents in foods: Mode of action and microbial resistance mechanisms. *Int. J. Food Microbiol.* **50**, 1–17 (1999).

10. Ullmann *et al.* Pion scattering to collective excitations in 90Zr and 118Sn. *Phys. Rev. C, Nucl. Phys.* **35**, 1099–1113 (1987).

11. FUJISHIMA, A. & HONDA, K. Electrochemical Photolysis of Water at a Semiconductor Electrode. *Nature* **238**, 37–38 (1972).

12. Acar, C. & Dincer, I. 3.1 Hydrogen Production. in *Comprehensive Energy Systems* 1–40 (Elsevier, 2018). doi:10.1016/B978-0-12-809597-3.00304-7

13. El-Maghrabi, H. H. *et al.* Synthesis of mesoporous core-shell CdS@TiO_2 (0D and 1D) photocatalysts for solar-driven hydrogen fuel production. *J. Photochem. Photobiol. A Chem.* **351**, 261–270 (2018).

14. Sridharan, K. *et al.* Nanosheets for Photocatalytic Hydrogen Generation and Dye Silver Quantum Cluster (Ag9)-Grafted Graphitic Carbon Nitride Degradation. *Chem. - A Eur. J.* **21**, 9126–9132 (2015).

15. López, C. R. *et al.* Comparative study of alcohols as sacrificial agents in H_2 production by heterogeneous photocatalysis using Pt/TiO_2 catalysts. *J. Photochem. Photobiol. A Chem.* **312**, 45–54 (2015).

16. Tan, Y. *et al.* One-step synthesis of nanostructured $g\text{-}C_3N_4/TiO_2$ composite for highly enhanced visible-light photocatalytic H2 evolution. *Appl. Catal. B Environ.* **230**, 260–268 (2018).

17. Cao, B., Li, G. & Li, H. Hollow spherical $RuO_2@TiO_2@Pt$ bifunctional photocatalyst for coupled H2 production and pollutant degradation. *Appl. Catal. B Environ.* **194**, 42–49 (2016).

18. Khayatzadeh, J. & Abbasi, E. The effects of heavy metals on aquatic animals. *1st Int. Appl. Geol. Congr. Dep. Geol. Islam. Azad Univ. Branch, Iran* (2010).

19. Shah, M. Azo Dye Removal Technologies. *Austin J. Biotechnol. Bioeng.* **5**, 1090 (2018).

20. Allen, N. S. Photocatalysis: Science and Technology. *J. Photochem. Photobiol. A Chem.* **160**, 225 (2003).

21. Mamba, G. & Mishra, A. K. Graphitic carbon nitride ($g\text{-}C_3N_4$) nanocomposites: A new and exciting generation of visible light driven photocatalysts for environmental pollution remediation. *Applied Catalysis B: Environmental* **198**, (2016).

22. Zhang, G., Zhang, J., Zhang, M. & Wang, X. Polycondensation of thiourea into carbon nitride semiconductors as visible light photocatalysts. *J. Mater. Chem.* **22**, 8083–8091 (2012).

23. Thomas, A. *et al.* Graphitic carbon nitride materials: variation of structure and morphology and their use as metal-free catalysts. *J. Mater. Chem.* **18**, 4893 (2008).

24. Dong, G. & Zhang, L. Porous structure dependent photoreactivity of graphitic carbon nitride under visible light. *J. Mater. Chem.* **22**, 1160–1166 (2012).

25. Zhang, Y. *et al.* Porous graphitic carbon nitride synthesized via direct polymerization of urea for efficient sunlight-driven photocatalytic hydrogen production. *Nanoscale* **4**, 5300–5303 (2012).

26. Zhao, Z., Sun, Y. & Dong, F. Graphitic carbon nitride based nanocomposites: A review. *Nanoscale* **7**, 15–37 (2015).

27. Fu, J., Yu, J., Jiang, C. & Cheng, B. $g\text{-}C_3N_4$-Based Heterostructured Photocatalysts. *Advanced Energy Materials* **8**, 1–31 (2018).

28. Luo, J., Dong, G., Zhu, Y., Yang, Z. & Wang, C. Switching of semiconducting behavior from n-type to p-type induced high photocatalytic NO removal activity in $g\text{-}C_3N_4$. *Appl. Catal. B Environ.* **214**, 46–56 (2017).

29. Guo, W., Zhang, J., Li, G. & Xu, C. Enhanced photocatalytic activity of P-type (K, Fe) co-doped g-C_3N_4 synthesized in self-generated NH3 atmosphere. *Appl. Surf. Sci.* **470**, 99–106 (2018).

30. Jing, J., Chen, Z. & Feng, C. Dramatically enhanced photoelectrochemical properties and transformed p/n type of g-C_3N_4 caused by K and I co-doping. *Electrochim. Acta* **297**, 488–496 (2019).

31. Yuan, M., Voznyy, O., Zhitomirsky, D., Kanjanaboos, P. & Sargent, E. H. Synergistic Doping of Fullerene Electron Transport Layer and Colloidal Quantum Dot Solids Enhances Solar Cell Performance. 1–5 (2014). doi:10.1002/adma.201404411

32. Liu, G. *et al.* In Situ Bond Modulation of Graphitic Carbon Nitride to Construct p–n Homojunctions for Enhanced Photocatalytic Hydrogen Production. *Adv. Funct. Mater.* **26**, 6822–6829 (2016).

33. Cao, J. *et al.* Constructing nitrogen vacancy introduced g-C_3N_4 p-n homojunction for enhanced photocatalytic activity. *J. Environ. Chem. Eng.* **7**, 102984 (2019).

34. Li, Y. *et al. Carbon vacancy in C_3N_4 nanotube: Electronic structure, photocatalysis mechanism and highly enhanced activity*. *Applied Catalysis B: Environmental* **262**, (Elsevier B.V., 2020).

35. Tu, W. *et al.* Investigating the Role of Tunable Nitrogen Vacancies in Graphitic Carbon Nitride Nanosheets for Efficient Visible-Light-Driven H_2 Evolution and CO_2 Reduction. *ACS Sustain. Chem. Eng.* (2017). doi:10.1021/acssuschemeng.7b01477

36. Ruan, D., Kim, S., Fujitsuka, M. & Majima, T. Defects rich g-C_3N_4 with mesoporous structure for efficient photocatalytic H_2 production under visible light irradiation. *Appl. Catal. B Environ.* (2018). doi:10.1016/j.apcatb.2018.07.028

37. Dong, G., Jacobs, D. L., Zang, L. & Wang, C. Carbon vacancy regulated photoreduction of NO to N_2 over ultrathin g-C_3N_4 nanosheets. *Appl. Catal. B Environ.* **218**, 515–524 (2017).

38. Li, S. *et al.* Effective photocatalytic H_2O_2 production under visible light irradiation at g-C_3N_4 modulated by carbon vacancies. *Appl. Catal. B Environ.* **190**, 26–35 (2016).

39. Luo, W. *et al.* Pyrolysis of cellulose under ammonia leads to nitrogen-doped nanoporous carbon generated through methane formation. *Nano Lett.* **14**, 2225–2229 (2014).

40. Xu, J., Wang, Y. & Zhu, Y. Nanoporous graphitic carbon nitride with enhanced photocatalytic performance. *Langmuir* **29**, 10566–10572 (2013).

41. Liang, Q., Li, Z., Huang, Z. H., Kang, F. & Yang, Q. H. Holey Graphitic Carbon Nitride Nanosheets with Carbon Vacancies for Highly Improved Photocatalytic

Hydrogen Production. *Adv. Funct. Mater.* **25**, 6885–6892 (2015).

42. Wang, X. *et al.* 3D macropore carbon-vacancy g-C_3N_4 constructed using polymethylmethacrylate spheres for enhanced photocatalytic H2 evolution and CO2 reduction. *J. Energy Chem.* **53**, 139–146 (2020).

43. Li, J. *et al.* Carbon vacancies improved photocatalytic hydrogen generation of g-C3N4 photocatalyst via magnesium vapor etching. *Int. J. Hydrogen Energy* **45**, 13939–13946 (2020).

44. Ganesh, I. A review on magnesium aluminate ($MgAl_2O_4$) spinel : synthesis , processing and applications. (2016). doi:10.1179/1743280412Y.0000000001

45. Kong, H., Zhang, K., Zhang, J., Chai, Y. & Liu, C. Preparation selective hydrodesulfurization catalyst Co-Mo/$MgAl_2O_4$-Al_2O_3 for FCC gasoline. *Shiyou Xuebao, Shiyou Jiagong/Acta Pet. Sin. (Petroleum Process. Sect.* **26**, 499–505 (2010).

46. Nannan, S., Guowei, W., Dongmin, H. & Chunyi, L. Influence of V_2O_5loading on isobutane dehydrogenation on VO_x/$MgAl_2O_4$ catalyst. *Pet. Process. Petrochemicals* **45**, 45–49 (2014).

47. Nassar, M. Y., Ahmed, I. S. & Samir, I. A novel synthetic route for magnesium aluminate ($MgAl_2O_4$) nanoparticles using sol-gel auto combustion method and their photocatalytic properties. *Spectrochim. Acta - Part A Mol. Biomol. Spectrosc.* **131**, 329–334 (2014).

48. Soltani, T. & Entezari, M. H. Photolysis and photocatalysis of methylene blue by ferrite bismuth nanoparticles under sunlight irradiation. *J. Mol. Catal. A Chem.* **377**, 197–203 (2013).

49. Houas, A. *et al.* Photocatalytic degradation pathway of methylene blue in water. **31**, 145–157 (2001).

50. Sandoval, A., Hernández-Ventura, C. & Klimova, T. E. Titanate nanotubes for removal of methylene blue dye by combined adsorption and photocatalysis. *Fuel* **198**, 22–30 (2017).

51. Gómez-Solís, C., Peralta-Arriaga, S. L., Torres-Martínez, L. M., Juárez-Ramírez, I. & Díaz-Torres, L. A. Photocatalytic activity of MAl_2O_4 (M = Mg, Sr and Ba) for hydrogen production. *Fuel* **188**, 197–204 (2017).

52. Wang, D., Zou, Z. & Ye, J. A new spinel-type photocatalyst $BaCr_2O_4$ for H_2 evolution under UV and visible light irradiation. *Chem. Phys. Lett.* **373**, 191–196 (2003).

53. Rekhila, G., Bessekhouad, Y. & Trari, M. Visible light hydrogen production on the novel ferrite $NiFe_2O_4$. *Int. J. Hydrogen Energy* **38**, 6335–6343 (2013).

54. Tang, J., Zou, Z. & Ye, J. Efficient photocatalytic decomposition of organic contaminants over $CaBi_2O_4$ under visible-light irradiation. *Angew. Chemie - Int. Ed.* **43**, 4463–4466 (2004).

55. Zeng, C. *et al.* Photocatalytic pure water splitting activities for $ZnGa_2O_4$ synthesized by various methods. *Mater. Res. Bull.* **61**, 481–485 (2015).

56. Zhang, X. *et al.* Photocatalytic decomposition of benzene by porous nanocrystalline $ZnGa_2O_4$ with a high surface area. *Environ. Sci. Technol.* **43**, 5947–5951 (2009).

57. Fu, Y. & Wang, X. Magnetically separable $ZnFe_2O_4$-graphene catalyst and its high photocatalytic performance under visible light irradiation. *Ind. Eng. Chem. Res.* **50**, 7210–7218 (2011).

58. Xu, X., Azad, A. K. & Irvine, J. T. S. Photocatalytic H_2 generation from spinels $ZnFe_2O_4$, $ZnFeGaO_4$ and $ZnGa_2O_4$. *Catal. Today* **199**, 22–26 (2013).

59. Lv, W. *et al.* Synthesis, characterization and photocatalytic properties of spinel $CuAl_2O_4$ nanoparticles by a sonochemical method. *J. Alloys Compd.* **479**, 480–483 (2009).

60. Vinosha, P. A., Mely, L. A., Jeronsia, J. E., Krishnan, S. & Das, S. J. Synthesis and properties of spinel $ZnFe_2O_4$ nanoparticles by facile co-precipitation route. *Optik (Stuttg).* **134**, 99–108 (2017).

61. Păcurariu, C. *et al.* New synthesis methods of $MgAl_2O_4$ spinel. *J. Eur. Ceram. Soc.* **27**, 707–710 (2007).

62. Troia, A., Pavese, M. & Geobaldo, F. Sonochemical preparation of high surface area $MgAl_2O_4$ spinel. *Ultrason. Sonochem.* **16**, 136–140 (2009).

63. Rondinone, A. J., Samia, A. C. S. & Zhang, Z. J. Superparamagnetic relaxation and magnetic anisotropy energy distribution in $CoFe_2O_4$ spinel ferrite nanocrystallites. *J. Phys. Chem. B* **103**, 6876–6880 (1999).

64. Sun, S. *et al.* Enhanced photocatalytic activity of sponge-like $ZnFe_2O_4$ synthesized by solution combustion method. *Prog. Nat. Sci. Mater. Int.* **22**, 639–643 (2012).

65. Maensiri, S., Sangmanee, M. & Wiengmoon, A. Magnesium ferrite ($MgFe_2O_4$) nanostructures fabricated by electrospinning. *Nanoscale Res. Lett.* **4**, 221–228 (2009).

66. Ahmed, A. A. A., Talib, Z. A., Hussein, M. Z. Bin & Zakaria, A. Improvement of the crystallinity and photocatalytic property of zinc oxide as calcination product of Zn-Al layered double hydroxide. *J. Alloys Compd.* **539**, 154–160 (2012).

67. Zhang, L. W., Wang, L. & Zhu, Y. F. Synthesis and performance of $BaAl_2O_4$ with a wide spectral range of optical absorption. *Adv. Funct. Mater.* **17**, 3781–3790 (2007).

68. Morita, K., Kim, B. N., Yoshida, H., Hiraga, K. & Sakka, Y. Spectroscopic study of the discoloration of transparent $MgAl_2O_4$ spinel fabricated by spark-plasma-sintering (SPS) processing. *Acta Mater.* **84**, 9–19 (2015).

69. Wang, S. *et al.* Synthesis and Characterization of $BaAl_2O_4$ Catalyst and its Photocatalytic Activity Towards Degradation of Methylene Blue Dye. *Zeitschrift fur Phys. Chemie* **233**, 1161–1181 (2019).

70. Pavese, A., Artioli, G., Pavese, A. & Hoser, A. $MgAl_2O_4$ synthetic spinel: Cation and vacancy distribution as a function of temperature, from in situ neutron powder diffraction. *Zeitschrift fur Krist.* **215**, 406–412 (2000).

71. Viezbicke, B. D., Patel, S., Davis, B. E. & Birnie, D. P. Evaluation of the Tauc method for optical absorption edge determination: ZnO thin films as a model system. *Phys. Status Solidi Basic Res.* **252**, 1700–1710 (2015).

72. Lasia, A. *Electrochemical Impedance Spectroscopy and its Applications*. *Electrochemical Impedance Spectroscopy and its Applications* **9781461489**, (Springer New York, 2014).

73. Jacobsson, T. J. & Edvinsson, T. Photoelectrochemical determination of the absolute band edge positions as a function of particle size for ZnO quantum dots. *J. Phys. Chem. C* **116**, 15692–15701 (2012).

74. Tan, K. A., Morad, N., Ooi, J. Q. & Active, P. Phytoremediation of Methylene Blue and Methyl Orange Using Eichhornia crassipes. *Int. J. Environ. Sci. Dev.* **7**, 724–728 (2016).

75. Ganguly, P. *et al.* 2D Nanomaterials for Photocatalytic Hydrogen Production. *ACS Energy Lett.* **4**, 1687–1709 (2019).

76. Wen, J., Xie, J., Chen, X. & Li, X. A review on g-C_3N_4-based photocatalysts. *Appl. Surf. Sci.* (2016). doi:10.1016/j.apsusc.2016.07.030

77. Jiang, J. *et al.* Dependence of electronic structure of g-C_3N_4 on the layer number of its nanosheets: A study by Raman spectroscopy coupled with first-principles calculations. *Carbon N. Y.* **80**, 213–221 (2014).

78. Jiang, L. *et al.* Passivated Perovskite Crystallization via g-C_3N_4 for High-Performance Solar Cells. **1705875**, 1–8 (2018).

79. Zhang, W., Zhang, Q., Dong, F. & Zhao, Z. The multiple effects of precursors on the properties of polymeric carbon nitride. *Int. J. Photoenergy* **2013**, (2013).

80. Fagan, R., McCormack, D. E., Hinder, S. J. & Pillai, S. C. Photocatalytic properties of g-C_3N_4-TiO_2 heterojunctions under UV and visible light conditions. *Materials (Basel).* **9**, 0–15 (2016).

81. Zinin, P. V *et al.* Ultraviolet and near-infrared Raman spectroscopy of graphitic C_3N_4 phase. *Chem. Phys. Lett.* **472**, 69–73 (2009).

82. Yuan, Y. *et al.* High-yield synthesis and optical properties of g-C_3N_4. *Nanoscale* **7**, 12343–12350 (2015).

83. Cao, S. *et al.* Sulfur-doped g-C_3N_4 nanosheets with carbon vacancies: General synthesis and improved activity for simulated solar-light photocatalytic nitrogen fixation. *Chem. Eng. J.* **353**, 147–156 (2018).

84. Wu, P., Wang, J., Zhao, J., Guo, L. & Osterloh, F. E. Structure defects in g-C_3N_4 limit visible light driven hydrogen evolution and photovoltage. *J. Mater. Chem. A* **2**, 20338–20344 (2014).

85. Ismael, M., Wu, Y., Taffa, D. H., Bottke, P. & Wark, M. Graphitic carbon nitride synthesized by simple pyrolysis: Role of precursor in photocatalytic hydrogen production. *New J. Chem.* **43**, 6909–6920 (2019).

86. Xu, J., Li, Y., Peng, S., Lu, G. & Li, S. Eosin Y-sensitized graphitic carbon nitride fabricated by heating urea for visible light photocatalytic hydrogen evolution: The effect of the pyrolysis temperature of urea. *Phys. Chem. Chem. Phys.* **15**, 7657–7665 (2013).

87. Cao, J. *et al.* Solid-state method synthesis of SnO_2-decorated g-C_3N_4 nanocomposites with enhanced gas-sensing property to ethanol. *Materials (Basel).* **10**, 1–14 (2017).

88. Jiang, D. *et al.* N-doped graphene quantum dots as an effective photocatalyst for the photochemical synthesis of silver deposited porous graphitic C_3N_4 nanocomposites for nonenzymatic electrochemical H_2O_2 sensing. *RSC Adv.* **4**, 16163–16171 (2014).

89. Huang, D. *et al.* Graphitic Carbon Nitride-Based Heterojunction Photoactive Nanocomposites : Applications and Mechanism Insight. *ACS Appl. Mater. Interfaces* **10**, 21035–21055 (2018).

90. Wen, Y. *et al.* Defective g-C_3N_4 prepared by the $NaBH_4$ reduction for high-performance H_2 production. *ACS Sustain. Chem. Eng.* **7**, 2343–2349 (2019).

91. Kachian, J. S. & Bent, S. F. Sulfur versus Oxygen Reactivity of Organic Molecules at the Ge(100)-2x1 Surface. *J. Am. Chem. Soc.* **131**, 7005–7015 (2009).

92. Niu, P., Qiao, M., Li, Y., Huang, L. & Zhai, T. Distinctive defects engineering in graphitic carbon nitride for greatly extended visible light photocatalytic hydrogen evolution. *Nano Energy* **44**, 73–81 (2018).

93. Mishra, A. *et al.* Graphitic carbon nitride (g–C_3N_4)–based metal-free photocatalysts for water splitting: A review. *Carbon N. Y.* **149**, 693–721 (2019).

94. Taveira, L. V., Montemor, M. F., Da Cunha Belo, M., Ferreira, M. G. & Dick, L. F. P. Influence of incorporated Mo and Nb on the Mott-Schottky behaviour of anodic films formed on AISI 304L. *Corros. Sci.* **52**, 2813–2818 (2010).

95. Swain, G., Sultana, S., Moma, J. & Parida, K. Fabrication of Hierarchical Two-Dimensional MoS_2 Nanoflowers Decorated upon Cubic $CaIn_2S_4$ Microflowers: Facile Approach to Construct Novel Metal-Free p-n Heterojunction Semiconductors with Superior Charge Separation Efficiency. *Inorg. Chem.* **57**, 10059–10071 (2018).

96. Naeem, R. *et al.* Single step aerosol assisted chemical vapor deposition of p-n Sn(II) oxide-Ti(IV) oxide nanocomposite thin film electrodes for investigation of photoelectrochemical properties. *New J. Chem.* **42**, 5256–5266 (2018).

97. Mumanga, T. J., Armando Diaz-Torres, L., Montes, E. & Gómez-Solís, C. MAl_2O_4 (M=Ba, Mg) photocatalytic activity dependence on annealing atmosphere. *Appl. Opt.* **59**, D246 (2020).

98. Liu, J., Huang, J., Zhou, H. & Antonietti, M. Uniform graphitic carbon nitride nanorod for efficient photocatalytic hydrogen evolution and sustained photoenzymatic catalysis. *ACS Appl. Mater. Interfaces* **6**, 8434–8440 (2014).

99. Sharma, R., Bisen, D. P., Shukla, U. & Sharma, B. G. X-ray diffraction: a powerful method of characterizing nanomaterials. *Recent Res. Sci. Technol.* **4**, 77–79 (2012).

100. Yang, D. *et al.* Chemical analysis of graphene oxide films after heat and chemical treatments by X-ray photoelectron and Micro-Raman spectroscopy. *Carbon N. Y.* **47**, 145–152 (2009).

101. Cheng, B., Fang, L., Zhang, Z., Xiao, Y. & Lei, S. $BaAl_2O_4:Eu^{2+}$, Dy^{3+} nanotube synthesis by heating conversion of homogeneous coprecipitates and afterglow characteristics. *J. Phys. Chem. C* **115**, 1708–1713 (2011).

102. Zheng, Y. *et al.* Ag/ZnO heterostructure nanocrystals: Synthesis, characterization, and photocatalysis. *Inorg. Chem.* **46**, 6980–6986 (2007).

103. Myers, H. P. Defects in Crystals. *Introd. Solid State Phys.* 75–78 (2002). doi:10.1119/1.1974472

104. Wang, C. *et al.* Effect of oxygen vacancy on enhanced photocatalytic activity of reduced ZnO nanorod arrays. *Appl. Surf. Sci.* **325**, 112–116 (2015).

105. Wu, Y. & Lu, G. The roles of density-tunable surface oxygen vacancy over bouquet-like Bi_2O_3 in enhancing photocatalytic activity. *Phys. Chem. Chem. Phys.* **16**, 4165–4175 (2014).

106. Parvarinezhad, S., Salehi, M. & Khademinia, S. Solid state synthesis of $MgAl_2O_4$ nanomaterials and solar light-induced photocatalytic removal of Malachite Green. *Int. J. Nano Dimens.* **10**, 89–104 (2018).

107. Sakai, R., Katsumata, T., Komuro, S. & Morikawa, T. Effect of composition on the phosphorescence from $BaAl_2O_4$: Eu^{2+}, Dy^{3+} crystals. *J. Lumin.* **85**, 149–154 (1999).

108. Aizawa, H., Komuro, S., Katsumata, T., Sato, S. & Morikawa, T. Long afterglow phosphorescent characteristics of $BaAl_2O_4$:Eu,Dy films. in *Thin Solid Films* **496**, 179–182 (2006).

109. Yang, J., Wang, D., Han, H. & Li, C. Roles of cocatalysts in photocatalysis and photoelectrocatalysis. *Acc. Chem. Res.* **46**, 1900–1909 (2013).

110. Ikreedeegh, R. R. & Tahir, M. A critical review in recent developments of metal-organic-frameworks (MOFs) with band engineering alteration for photocatalytic CO_2 reduction to solar fuels. *J. CO_2 Util.* **43**, 101381 (2021).

111. Yang, Y. *et al.* Double-sided modification of TiO_2 spherical shell by graphene sheets with enhanced photocatalytic activity for CO_2 reduction. *Appl. Surf. Sci.* **537**, 147991 (2021).

112. National Center for Biotechnology Information. Compound Summary for CID 8113, Diethanolamine. *PubChem* (2021).

113. Jones, C., Edens, M. R. & Lochary, J. F. Alkanolamines from Olefin Oxides and Ammonia. in *Kirk-Othmer Encyclopedia of Chemical Technology* (ed. D, G. M. & E.) (John Wiley and Sons, 2004).doi:10.1002/0471238961.0112110105040514.a01.pub2